
One-Time Soft Alignment Enables Resilient Learning without Weight Transport

Jeonghwan Cheon¹ Jaehyuk Bae¹ Se-Bum Paik¹

¹Department of Brain and Cognitive Sciences

Korea Advanced Institute of Science and Technology, Daejeon, Republic of Korea
{jeonghwan518, jaehyukbae, sbpaik}@kaist.ac.kr

Abstract

Backpropagation is the cornerstone of deep learning, but its reliance on symmetric weight transport and global synchronization makes it computationally expensive and biologically implausible. Feedback alignment offers a promising alternative by approximating error gradients through fixed random feedback, thereby avoiding symmetric weight transport. However, this approach often struggles with poor learning performance and instability, especially in deep networks. Here, we show that a one-time soft alignment between forward and feedback weights at initialization enables deep networks to achieve performance comparable to backpropagation, without requiring weight transport during learning. This simple initialization condition guides stable error minimization in the loss landscape, improving network trainability. Spectral analyses further reveal that initial alignment promotes smoother gradient flow and convergence to flatter minima, resulting in better generalization and robustness. Notably, we also find that allowing moderate deviations from exact weight symmetry can improve adversarial robustness compared to standard backpropagation. These findings demonstrate that a simple initialization strategy can enable effective learning in deep networks in a biologically plausible and resource-efficient manner.

1 Introduction

Recent breakthroughs in artificial intelligence have been driven by a powerful learning rule, backpropagation [1, 2]. Leveraging this method, modern large-scale deep networks have achieved superhuman performance in domains such as image recognition [3, 4] and language modeling [5, 6]. Despite its effectiveness, backpropagation faces significant challenges in terms of computational and resource efficiency [7–9]. For instance, training a single large language model can consume over a thousand megawatt-hours of electricity [10] and emit tens of tons of carbon dioxide [11], raising concerns about its sustainability. This heavy energy consumption largely stems from a core limitation of backpropagation: it requires dynamic access to separate memory units during learning [7, 12, 13].

In contrast to backpropagation on von Neumann architectures [14, 15] —which requires dynamic memory access between separate compute and storage units — the biological brain learns through locally connected, physically fixed neurons [16]. This fundamental difference raises two key questions: How does the brain learn efficiently using only local connections? And how can we replicate such energy-efficient learning in artificial systems? These questions have motivated interest in biologically plausible deep learning and neuromorphic computing as promising alternatives [17, 18]. Unlike backpropagation, which depends on symmetric forward and backward pathways, biological neural circuits rely on distinct feedforward and feedback connections [19, 20]. However, how the brain learns using such asymmetric pathways remains an open challenge, known as the weight transport problem [21–25].

Notably, feedback alignment algorithms address the weight transport problem by using fixed, random synaptic feedback [23]. It demonstrates that networks can learn without explicitly copying forward weights into the backward pass. During training, forward weights gradually “align” with the fixed random feedback weights, approximating the error signals of backpropagation. While this offers a biologically plausible mechanism with separate feedforward and feedback pathways, its performance — especially in deep networks — remains significantly below that of standard backpropagation and fails to explain the brain’s remarkable learning efficiency [26].

Recent approaches have proposed biologically plausible learning rules that begin to close this performance gap, yet they still grapple with the weight transport problem. For example, the sign-symmetry algorithm communicates only the sign of each weight, rather than its full value, but still requires sign information to be transmitted during learning [27, 28]. Predictive coding [29, 30] and equilibrium propagation [31] provide compelling energy-based frameworks but rely on perfectly symmetric forward and backward weights — effectively assuming exact synaptic mirroring. Other methods, such as weight mirror and the Kolen–Pollack algorithm [32, 33] adapt the feedback pathway to promote weight alignment, but at the cost of additional bidirectional connections — an arrangement that lacks biological plausibility. In short, these methods partially replace weight transport with constrained or adaptive feedback, but still depend on sign transmission, tied weights, or added connectivity throughout learning.

Here, we propose a different approach to biologically plausible learning, focusing on soft alignment at initialization rather than enforcing symmetry throughout training. We show that aligning forward and backward weights once at initialization, without any weight transport thereafter, is sufficient to guide learning. This initial alignment shapes the learning dynamics, enabling convergence to a smoother loss landscape and improving trainability, generalization, and robustness. Furthermore, our method demonstrates superior adversarial robustness compared to standard backpropagation.

Overall, these results identify a minimal yet effective requirement for biologically plausible networks to approach backpropagation-level performance, while offering a computationally efficient solution to the credit assignment problem in neural computation.

2 Preliminaries

2.1 Credit assignment and backpropagation

To optimize a network to perform a given task — to enable learning — each neuron must adjust its synaptic weights in a way that reduces the discrepancy between its actual and expected outputs. This, in turn, requires assigning an appropriate portion of the overall error to each weight, a challenge known as the credit assignment problem. In machine learning, backpropagation [1] offers an effective solution to this problem and has become the standard method for training artificial neural networks.

Concretely, consider a typical multi-layer feedforward network for pattern classification, denoted as $f_\theta : \mathbb{R}^m \rightarrow \mathbb{R}^d$, parameterized by $\theta = \{\mathbf{W}_l, \mathbf{b}_l\}_{l=0}^{L-1}$. Given an input $\mathbf{x} \in \mathbb{R}^m$, the network computes its output through the forward pass:

$$\mathbf{o}_{l+1} = \mathbf{W}_l \mathbf{h}_l + \mathbf{b}_l, \quad \mathbf{h}_{l+1} = \phi(\mathbf{o}_{l+1}), \quad (1)$$

where \mathbf{W}_l denotes the forward weight matrix at layer l , \mathbf{b}_l is the corresponding bias vector. The signal is propagated through a nonlinear activation function ϕ . Once the forward pass is complete, the loss is computed as the discrepancy between the network’s output and the ground-truth labels. Backpropagation then calculates the gradient of this loss with respect to each weight and bias, and these gradients are subsequently used to update the network parameters.

$$\delta_l = \frac{\partial \mathcal{L}}{\partial \mathbf{o}_l} = (\mathbf{W}_l^T \delta_{l+1}) \odot \phi'(\mathbf{o}_l), \quad (2)$$

where δ_l denotes the error signal at layer l , ϕ' represents the derivative of the activation function, and \odot indicates the element-wise product. Based on this error signal, the weights are updated as

$$\Delta \mathbf{W}_l = -\eta \delta_{l+1} \mathbf{h}_l^T, \quad (3)$$

where η denotes the learning rate.

2.2 Weight transport problem and feedback alignment

Although backpropagation endows neural networks with powerful learning capabilities, it relies on exact knowledge of the forward weights in the next layer to compute the backward error signal — known as the weight transport problem [21, 22] — which underlies both its energy inefficiency and its lack of biological plausibility.

Feedback alignment [23] offers a more biologically plausible alternative by replacing the backward-pathway weights with fixed, random matrices \mathbf{B}_l , thereby eliminating the need for weight transport:

$$\delta_l = \frac{\partial \mathcal{L}}{\partial \mathbf{o}_l} = (\mathbf{B}_l \delta_{l+1}) \odot \phi'(\mathbf{o}_l). \quad (4)$$

Since feedback alignment substitutes the core backpropagation operation — the use of the transpose of the forward weights \mathbf{W}_l — with a random, fixed matrix \mathbf{B}_l , the resulting error signal is initially uninformative. However, during training, the forward weights \mathbf{W}_l gradually adapt to “align” with the fixed \mathbf{B}_l^\top . This emergent alignment causes the error signals (4) to approximate those computed by backpropagation (2).

3 One-time initial feedback alignment

Algorithm 1 Feedback alignment with initial weight alignment

```

1: procedure INITIALIZATION WITH SOFT INITIAL ALIGNMENT(network  $f_\theta, \theta_{init}$ )
2:   for layer  $l = L-1$  to 0 do
3:      $\mathbf{B}_l \sim \mathcal{N}(0, \frac{\sigma^2}{fan_{in}})$  ▷ initialize backward weights
4:      $\mathbf{W}_l = \mathbf{B}_l^\top \cos(\theta_{init}) + \mathbf{R} \sin(\theta_{init}), \mathbf{R} \sim \mathcal{N}(0, \frac{\sigma^2}{fan_{in}})$  ▷ initialize forward weights
5: procedure FEEDBACK ALIGNMENT(network  $f_\theta, \text{data}$ )
6:   for each epoch do
7:     for each batch =  $(\mathbf{x}, \mathbf{y}) \in \text{data}$  do
8:        $\mathcal{L}(\theta) = \text{Loss}(f_\theta(\mathbf{x}), \mathbf{y})$  ▷ forward pass, equation (1)
9:        $\delta_L = \frac{\partial \mathcal{L}}{\partial \mathbf{o}_L}$  ▷ compute error
10:      for layer  $l = L-1$  to 0 do
11:         $\mathbf{W}_l = \mathbf{W}_l - \eta \delta_{l+1} \mathbf{h}_l^\top$  ▷ update weights, equation (3)
12:         $\delta_l = (\mathbf{B}_l \delta_{l+1}) \odot \phi'(\mathbf{o}_l)$  ▷ compute error, equation (4)

```

Even though feedback alignment eliminates the need for exact weight transport, its performance remains significantly inferior to that of standard backpropagation. In this work, we propose that imposing a soft initial alignment between forward and backward weights can dramatically improve biologically plausible deep learning. Unlike earlier schemes that rely on sign-constrained feedback or maintain a strict coupling between forward and backward weights throughout training, our method requires soft alignment only at initialization, after which the forward and backward weights are allowed to evolve independently. Concretely, we initialize the forward weights \mathbf{W}_l to match the fixed random backward weights \mathbf{B}_l directly or align with them in a “soft” sense via a projection (Algorithm 1). In contrast to baseline feedback alignment, our method begins training with an aligned configuration between forward and backward weights—yet it never requires further synchronization during learning.

We proposed initial alignment as a means to improve neural computation without requiring explicit weight transport during learning. Importantly, there are biologically plausible mechanisms through which such an initialization condition could arise during development. Recent studies have shown that mimicking the brain’s developmental process [34–37], for example, through pretraining with random noise can yield weight alignment, thereby providing a “soft” alignment when the network begins learning from real data [38]. Similarly, other work has demonstrated that sign symmetry can emerge through ligand-specific axonal guidance during wiring of forward- and feedback-projecting neurons [27]. Although initial alignment itself may not be strictly biologically plausible, these findings suggest that such alignment could arise naturally during development.

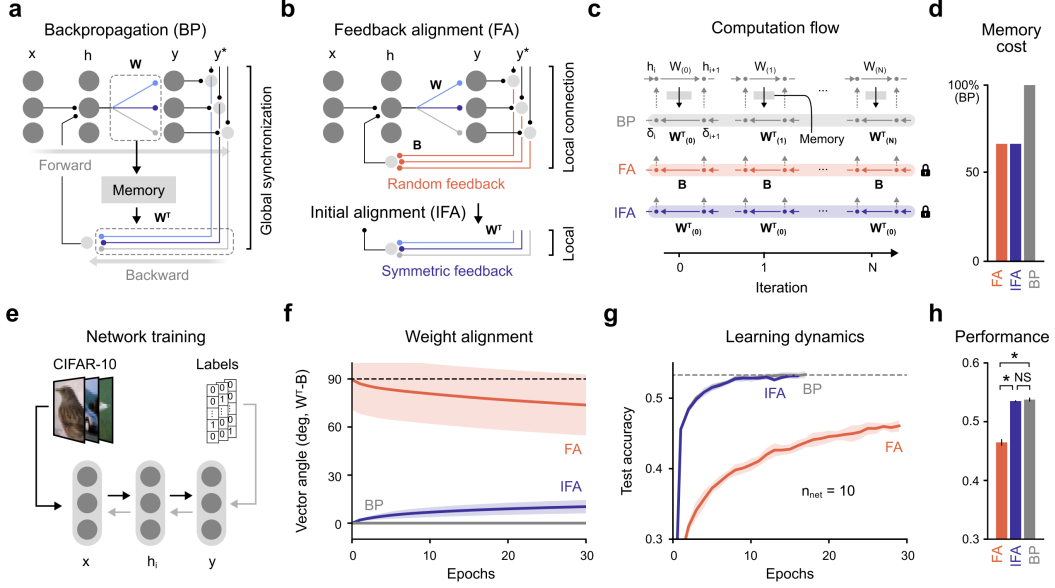


Figure 1: Effect of initial weight alignment on learning without weight transport. (a) Schematic of the backpropagation (BP) algorithm, where forward and backward weights are kept synchronized during training through external memory access. (b) Schematic of feedback alignment (FA) algorithms, which use a separate backward pathway with fixed, random feedback weights. Initial feedback alignment (IFA) also uses fixed feedback weights but aligns them with the forward weights only at initialization. (c) Computation flow for implementing backpropagation and feedback alignment on-chip. (d) Comparison of memory access cost between FA and BP. (e) Neural network models trained on the CIFAR-10 dataset using various learning algorithms. (f) Alignment angle between forward and backward weights in the final layer of the network. (g) Learning curves showing test accuracy over the course of training. (h) Final test accuracy.

4 Results

4.1 One-time initial alignment enables learning without weight transport

To compare the effect of initial alignment, we investigated neural network learning under three different feedback dynamics while keeping all other conditions constant. Backpropagation (BP) is the standard training algorithm, in which the forward weights are copied to the backward path at every iteration to compute gradients (Figure 1a). We also tested feedback alignment (FA), a biologically plausible alternative that avoids the weight transport problem by employing fixed, random feedback weights (Figure 1b). Our proposed model, initial feedback alignment (IFA), adopts the same feedback pathway as FA but differs at initialization: the backward weights are set equal to the forward weights at the start of training (Figure 1c). Like FA, IFA requires no weight transport during training and can be implemented with local circuits, and it requires a one-time initial alignment. We compared the computational flow of these three feedback dynamics (Figure 1d). In BP, forward weights must be copied into memory and accessed during each backward pass. In contrast, both FA and IFA use fixed feedback weights throughout training, eliminating the need for per-iteration weight transport or memory access. As a result, their memory-access overhead is significantly lower than that of BP (Figure 1d).

To compare these learning algorithms, we trained multi-layer feedforward networks on a natural image classification task using three distinct feedback schemes (Figure 1e). To characterize their learning dynamics, we first measured the alignment between forward and backward weights (Figure 1f) by computing the cosine similarity of corresponding weight vectors. As expected, BP maintains exact symmetry: forward and backward weights are identical because each forward weight is stored and retrieved during the backward pass. In FA, fixed random feedback weights gradually induce alignment in the forward weights during training. In contrast, IFA begins with forward weights set equal to the backward weights and then gradually relaxes this alignment during learning. We next examined the learning curves for each feedback scheme (Figure 1g). Remarkably, IFA's convergence

trajectory closely mirrors that of BP: it learns substantially faster than baseline FA and ultimately achieves performance comparable to BP. Indeed, final accuracy under IFA is significantly higher than under FA (Figure 1g, right; FA vs. IFA, $n_{\text{net}} = 10$, two-sided rank-sum test, $P < 10^{-3}$) and not significantly different from BP (BP vs. IFA, $n_{\text{net}} = 10$, two-sided rank-sum test, NS, $P = 0.082$). These findings suggest that a one-time alignment of forward and feedback weights at initialization is sufficient to enable learning performance comparable to BP, without requiring ongoing synchronization throughout training.

In addition, we evaluated test accuracy under various conditions to assess the effect of initial weight alignment. Using several standard image classification benchmarks — including SVHN [39], CIFAR-10, CIFAR-100 [40] and STL-10 [41] — we found that initializing forward and backward weights consistently leads to improved test accuracy. We further extended our experiments to convolutional neural network (CNN) architectures [3, 42], confirming that this initialization strategy enhances learning performance even without any weight-transport during training.

4.2 Stabilizing learning through initial weight alignment

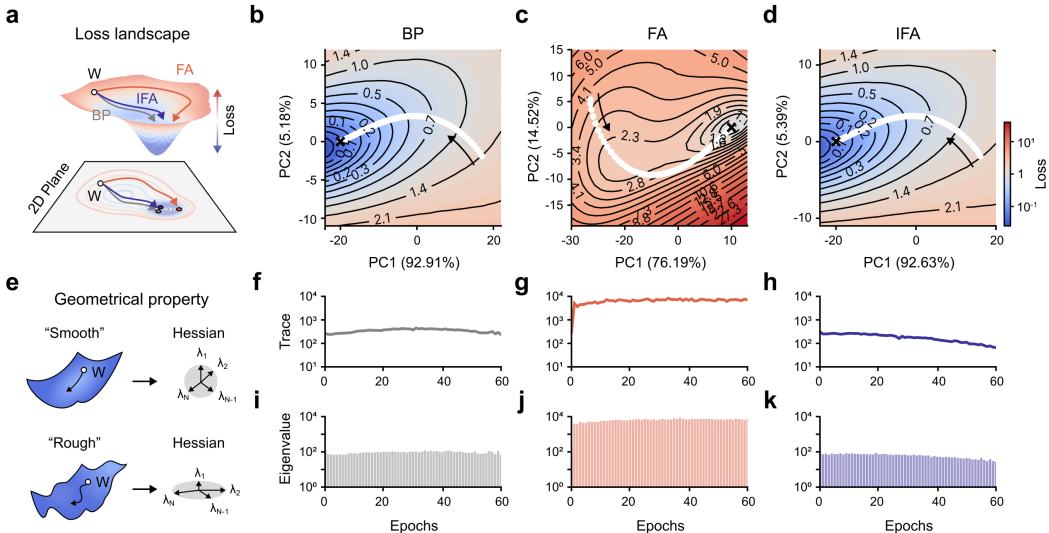


Figure 2: Loss landscape analysis of learning trajectories under different training rules. (a) Illustration of neural networks traversing the loss landscape during training, with each trajectory corresponding to a different learning algorithm. (b-d) Training trajectories projected onto a two-dimensional subspace defined by the first two principal components (PCA): (b) BP, (c) FA, (d) IFA. (e) Geometric properties of the loss landscape, quantified using the Hessian’s spectrum; smoother landscapes exhibit narrower spectra (i.e., smaller spectral radius). (f-h) Trace of the Hessian over the course of training. (i-k) Maximum eigenvalue of the Hessian during training for BP, FA, and IFA, respectively.

Next, we examined how initial alignment influences learning dynamics within the loss landscape, using principal component analysis [43] (Figure 2a) to visualize training trajectories. Specifically, we compared the trajectories produced under three feedback dynamics: BP (Figure 2b), FA (Figure 2c), and IFA (Figure 2d). BP exhibits stable and directed trajectories that effectively converge toward the global minimum. In contrast, FA results in more erratic trajectories — longer and less direct — indicating inefficient navigation of the loss landscape. Notably, IFA produces stable trajectories and a loss landscape structure that closely resemble those of BP, suggesting that initial alignment facilitates more efficient and stable learning.

To quantitatively compare the learning trajectories under different feedback dynamics, we performed a spectral analysis of the loss Hessian [44]. Specifically, we assessed the smoothness of the loss landscape (Figure 2e) by measuring the trace of the Hessian (Figure 2f–h) and its maximum eigenvalue (Figure 2i–k). Consistent with our trajectory-based observations, BP maintains low Hessian trace and top eigenvalue throughout training, indicating a smooth loss surface. In contrast, FA exhibits substantially higher trace and top eigenvalue, suggesting a much rougher landscape. Notably, IFA preserves low Hessian trace and top eigenvalues across the entire learning process. These results

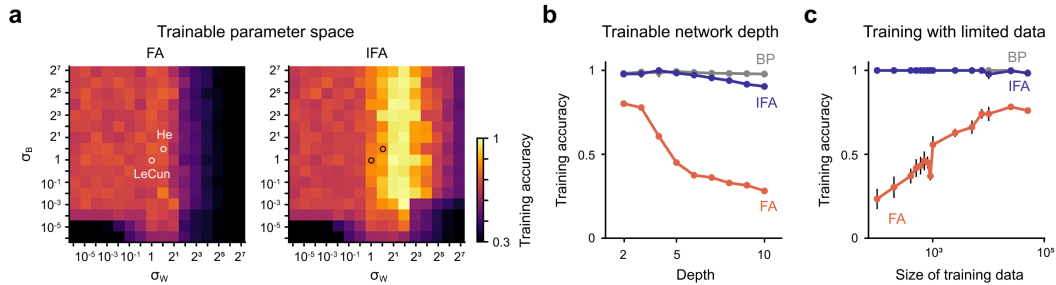


Figure 3: Trainability of neural networks under various conditions. (a) Trainable parameter space: the x- and y-axes represent the variances of the forward and backward weights, respectively. Color indicates the final training accuracy. The point (1, 1) corresponds to LeCun initialization; $(\sqrt{2}, \sqrt{2})$ corresponds to He initialization. (b) Trainability versus network depth: final training accuracy for feedforward networks with depths ranging from 2 to 10 layers. (c) Trainability under limited data: final training accuracy as a function of training set sizes, ranging from 100 to 50,000 samples.

suggest that providing initial guidance for error minimization is sufficient to promote stable learning dynamics and a smooth optimization trajectory, even in the absence of ongoing weight transport.

Building on the observation that stable learning induced by initial alignment between forward and backward weights governs the entire training process, we hypothesized that this alignment enhances neural network trainability under various conditions. First, we investigated networks initialized with different combinations of forward and backward weight variances (Figure 3a). Next, we examined how initial alignment influences the maximum trainable depth (Figure 3b). In baseline FA, trainability rapidly degrades as depth increases, whereas IFA enables training at greater depths, comparable to those achievable with backpropagation. Finally, we considered a limited-data regime (Figure 3c). Because FA must learn to approximate backpropagation from data, it fails when the dataset is too small. In contrast, IFA enables successful training even under severe data constraints, achieving performance comparable to BP.

4.3 Initial alignment enhances robust generalization

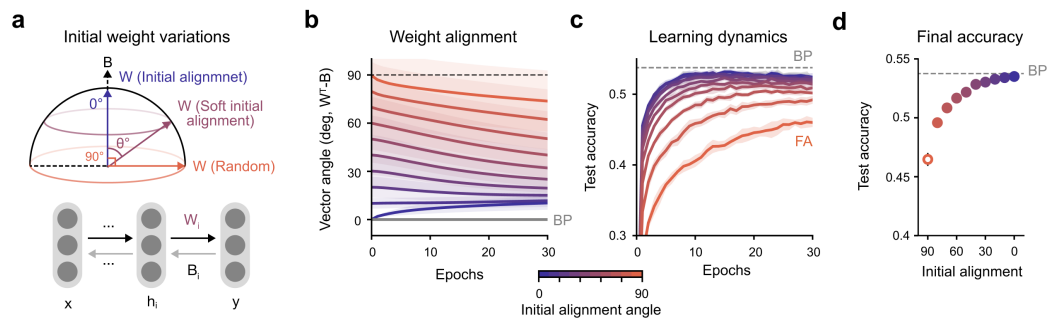


Figure 4: Effect of the degree of initial alignment on network performance. (a) Schematic of initialization conditions for forward and backward weights in feedback alignment. Perfect initial alignment sets the backward weights equal to the forward weights at initialization, whereas baseline feedback alignment uses randomly initialized backward weights. Soft alignment is achieved by sampling forward weights within a subspace defined by a specified angle relative to the backward weights. (b) Angle between forward and backward weights over the course of training. (c) Learning curves showing test accuracy during training. (d) Relationship between the initial alignment angle and final test accuracy.

To evaluate the impact of initial alignment, we systematically varied the alignment angle between forward and backward weights and analyzed the resulting learning dynamics (Figure 4a). An initial angle of 0° indicates perfect alignment, where forward and backward weights are identical, while an angle of 90° corresponds to orthogonal weights, as in baseline feedback alignment. Intermediate (“soft”) alignments were generated by projecting the forward weights onto a subspace defined by

a specific angle relative to the backward weights. We found that the learning dynamics depend strongly on the initial alignment (Figure 4b). When the initial alignment is strong, learning proceeds by gradually relaxing this alignment; when the initial alignment is weak, the network learns by progressively aligning the weights. The learning curves reflect this behavior (Figure 4c): stronger initial alignment leads to faster convergence and higher final test accuracy. Plotting the final test accuracy as a function of the initial alignment angle (Figure 4d) reveals a trend — performance improves with stronger alignment but eventually saturates. These results suggest that while a good initial alignment is critical for effective learning, perfect symmetry between forward and backward weights is not necessary.

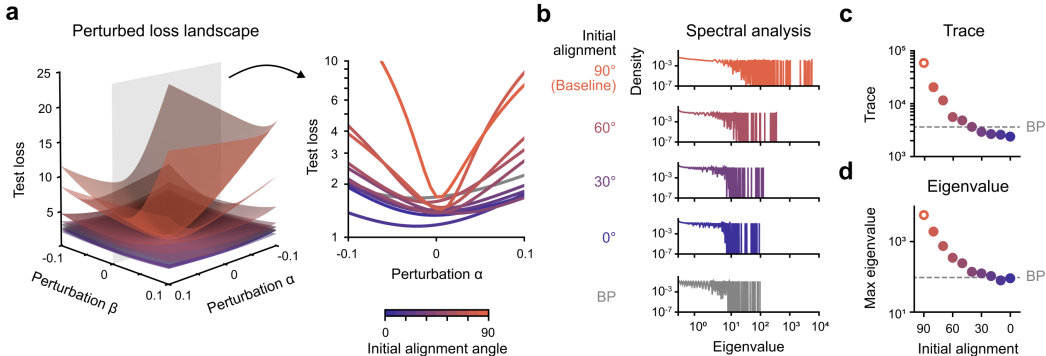


Figure 5: Spectral analysis of convergence across initial alignment angles. (a) Loss landscape visualized by perturbing the trained model parameters within a two-dimensional subspace defined by the top two eigenvectors of the Hessian. The axes, denoted by α and β , represent scaling factors for perturbations along the first and second eigenvector directions, respectively. The landscapes are color-coded according to each network’s initial alignment angle. (b) Spectral density of the Hessian eigenvalues, illustrating the distribution of curvature across the parameter space. (c) Relationship between the initial alignment angle and the trace of the Hessian. (d) Relationship between the initial alignment angle and the largest Hessian eigenvalue.

Next, we performed a spectral analysis of the converged optima obtained under varying initial alignment angles. Specifically, we visualized the loss landscape by perturbing the model parameters along two principal directions (Figure 5a), defined by the eigenvectors corresponding to the largest and second-largest eigenvalues of the Hessian. The baseline FA method exhibits a rough loss landscape, where even small perturbations in parameter space lead to significant increases in loss. In contrast, applying a soft initial alignment dramatically smooths the loss landscape of the converged optima, making it comparable to that observed with backpropagation. Furthermore, increasing the degree of initial weight alignment leads to progressively smoother loss landscapes.

Additionally, we validated this trend by analyzing the spectral density of Hessian eigenvalues (Figure 5b). Under baseline FA, the spectrum is shifted toward higher eigenvalues and exhibits greater dispersion compared to BP. Introducing initial alignment compresses the spectrum, resulting in a distribution that closely matches that of BP. To quantify the smoothness of the loss landscape, we computed both the Hessian trace (Figure 5c) and its largest eigenvalue (Figure 5d). Both metrics decrease as the initial alignment angle increases, and then plateau beyond a certain alignment threshold. These geometric insights align with our earlier observation that test accuracy improves and then saturates with stronger initial alignment (Figure 4d). Collectively, these findings indicate that initial weight alignment plays a critical role in shaping a smooth loss landscape — a known factor in promoting robust generalization [45–49]. Notably, only a moderate degree of alignment is necessary to obtain these benefits.

The spectral analysis revealed that initial weight alignment promotes convergence to a smoother loss landscape. Prior work has suggested that smoother loss landscape reduce a network’s sensitivity to input distortions or perturbations [49], implying that initial weight alignment may enhance robustness. To test this hypothesis, we employed a benchmark image dataset featuring fifteen corruption types, categorized into noise, blur, weather, and digital distortions [50] (Figure 6a). We trained networks using feedback dynamics across varying initial alignment angles and evaluated their classification accuracy on the corrupted inputs (Figure 6b). Notably, increasing the degree of initial alignment

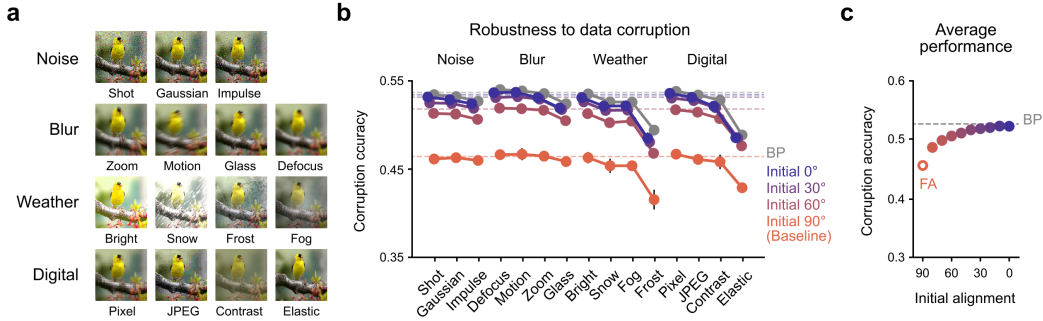


Figure 6: Effect of initial weight alignment on corruption robustness. (a) Fifteen image corruption types, grouped into four categories — noise, blur, weather, and digital — were applied to test samples to evaluate network robustness. (b) Classification accuracy on corrupted inputs (solid lines with markers) compared to accuracy on clean, uncorrupted images (dotted lines). (c) Relationship between the initial alignment angle and robustness, measured as the average accuracy across all corruption types.

consistently improved test accuracy across all corruption types (Figure 6c). Furthermore, when the severity of each corruption was gradually increased, networks with stronger initial alignment exhibited greater resistance to these progressively challenging distortions. These results suggest that initial weight alignment, by promoting a smoother loss landscape, ultimately enhances the robustness of the network.

4.4 The role of weight misalignment in promoting adversarial robustness

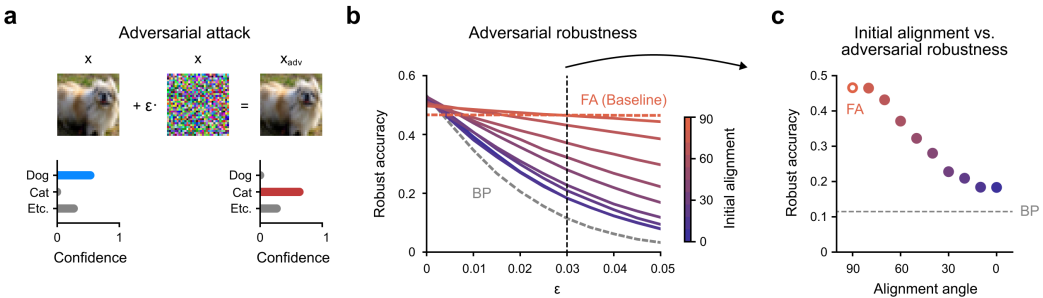


Figure 7: Effect of weight misalignment on adversarial robustness. (a) Illustration of an adversarial attack: small, targeted perturbations are added to input images to induce misclassification. (b) Classification accuracy as a function of increasing adversarial perturbation strength. (c) Relationship between the initial alignment angle and adversarial robustness, measured as classification accuracy under attack with perturbation magnitude $\epsilon = 0.03$.

Thus far, we have emphasized that stronger initial weight alignment enhances standard training performance. Conversely, we also demonstrate that weight misalignment can confer benefits in the context of adversarial robustness. To evaluate this, we conducted adversarial attacks using the Fast Gradient Sign Method (FGSM) (Figure 7a), which applies gradient-based perturbations to input images to induce misclassification [51]. Under standard BP, model accuracy rapidly deteriorates as the perturbation strength increases (Figure 7b, BP). In contrast, models trained with IFA maintain significantly higher accuracy, even under stronger attacks (Figure 7b, IFA). This robustness appears to emerge from the gradual “loosening” of weight alignment that naturally occurs during fixed-feedback learning, which reduces the impact of adversarial perturbations. Furthermore, we observed that larger initial misalignment further improves adversarial robustness (Figure 7c). Taken together, these findings highlight a functional advantage of weight misalignment and underscore the practical benefits of employing “soft” alignment at initialization.

5 Discussion

We demonstrated that initial soft alignment can effectively guide backpropagation-like learning, even without enforcing weight transport between forward and backward pathways throughout training. Specifically, soft alignment at initialization facilitates stable convergence to flatter optima, leading to improved generalization and robustness. Interestingly, we also identified a functional benefit of misalignment: enhanced adversarial robustness compared to standard backpropagation. Overall, these findings present a simple yet powerful pathway toward biologically plausible deep learning.

Critical role of initial conditions in learning dynamics. Traditional backpropagation algorithms rely on exact symmetry between forward and backward weights throughout training. In contrast, we show that soft alignment imposed only at initialization is sufficient to achieve backpropagation-like learning in terms of performance, robustness, and stability. This finding suggests that a one-time, approximate alignment of weights at the start of training can support error-driven learning without requiring explicit weight transport during the training process. Supporting this view, prior studies have shown that initialization plays a pivotal role in neural network behavior, influencing accuracy [52–55] and calibration [56]. Collectively, these results highlight the fundamental role of initial conditions in shaping the learning dynamics and functional development of neural networks.

Developmental foundations of biologically plausible weight alignment. Unlike artificial neural networks, which typically require externally provided datasets for training, the biological brain begins learning even before birth as it is exposed to sensory inputs [34–37]. During this prenatal stage, spontaneous neural activity — often resembling random noise — drives the formation and refinement of synaptic connections. Notably, prior work has shown that pretraining neural networks using random noise inputs can promote alignment between forward and backward weights under feedback alignment algorithm [38]. This suggests that spontaneous activity-dependent refinement may serve as a developmental mechanism for establishing soft initial weight alignment. Furthermore, cell-type-specific axonal guidance mediated by chemical ligands may contribute to forming feedforward and feedback circuits with initial symmetry in weight signs [27].

Initialization strategies for neuromorphic computing. In neuromorphic hardware systems [17, 18] and physical neural networks [57, 58], initializing weight alignment between forward and backward pathways offers a simple yet effective strategy to support learning. From an implementation perspective, this approach imposes minimal overhead: backward weights can be initialized as a mirror of forward weights directly within on-chip memory, requiring no additional memory allocation or computation overhead. Despite its simplicity, our findings suggest that this initialization method can promote stable learning dynamics and achieve performance comparable to standard backpropagation, without incurring costly weight transport or frequent memory read/write operations typically required.

6 Broader impacts and limitations

Broader impacts. One of the most pressing challenges in artificial intelligence today is energy inefficiency. As model sizes increase and AI systems are deployed across a wide range of applications, the associated electricity consumption and carbon emissions have raised serious concerns about the long-term sustainability of current approaches. Biologically plausible learning rules that avoid explicit weight transport offer a promising path toward more energy-efficient computation. Our findings can be leveraged in neuromorphic hardware to reduce power consumption and environmental impact, thereby contributing to the development of more sustainable AI technologies.

Limitations. This study primarily focused on multi-layer feedforward networks and evaluated performance using standard benchmark tasks. We also extended our experiments to convolutional architectures and found that initial weight alignment consistently improves the performance of feedback alignment. However, a performance gap remains between our approach and full backpropagation in deeper or more complex models. Therefore, while our method offers a simple and hardware-friendly mechanism to improve learning without requiring weight transport, it does not yet match the accuracy of conventional backpropagation.

7 Code availability

Python 3.12 (Python Software Foundation) with PyTorch 2.1 was used to perform the simulation. The code used in this work will be made available after the paper is published.

Acknowledgments and Disclosure of Funding

This work was supported by the National Research Foundation of Korea (NRF) grants (NRF2022R1A2C3008991 to S.P.) and by the Singularity Professor Research Project of KAIST (to S.P.).

References

- [1] David E. Rumelhart, Geoffrey E. Hinton, and Ronald J. Williams. Learning representations by back-propagating errors. *Nature*, 323:533–536, 10 1986.
- [2] Yann LeCun, Yoshua Bengio, and Geoffrey Hinton. Deep learning. *Nature*, 521(7553):436–444, 2015.
- [3] Alex Krizhevsky, Ilya Sutskever, and Geoffrey E Hinton. Imagenet classification with deep convolutional neural networks. *Advances in Neural Information Processing Systems*, 25, 2012.
- [4] Kaiming He, Xiangyu Zhang, Shaoqing Ren, and Jian Sun. Deep residual learning for image recognition. In *Proceedings of the IEEE conference on computer vision and pattern recognition*, pages 770–778, 2016.
- [5] Josh Achiam, Steven Adler, Sandhini Agarwal, Lama Ahmad, Ilge Akkaya, Florencia Leoni Aleman, Diogo Almeida, Janko Altenschmidt, Sam Altman, Shyamal Anadkat, et al. Gpt-4 technical report. *arXiv preprint arXiv:2303.08774*, 2023.
- [6] Gemini Team, Rohan Anil, Sebastian Borgeaud, Jean-Baptiste Alayrac, Jiahui Yu, Radu Soricut, Johan Schalkwyk, Andrew M Dai, Anja Hauth, Katie Millican, et al. Gemini: a family of highly capable multimodal models. *arXiv preprint arXiv:2312.11805*, 2023.
- [7] Emma Strubell, Ananya Ganesh, and Andrew McCallum. Energy and policy considerations for modern deep learning research. In *Proceedings of the AAAI conference on artificial intelligence*, volume 34, pages 13693–13696, 2020.
- [8] Vivienne Sze, Yu-Hsin Chen, Tien-Ju Yang, and Joel S Emer. Efficient processing of deep neural networks: A tutorial and survey. *Proceedings of the IEEE*, 105(12):2295–2329, 2017.
- [9] Roy Schwartz, Jesse Dodge, Noah A Smith, and Oren Etzioni. Green ai. *Communications of the ACM*, 63(12):54–63, 2020.
- [10] David Patterson, Joseph Gonzalez, Quoc Le, Chen Liang, Lluís-Miquel Munguia, Daniel Rothchild, David So, Maud Texier, and Jeff Dean. Carbon emissions and large neural network training. *arXiv preprint arXiv:2104.10350*, 2021.
- [11] Alexandra Sasha Luccioni, Sylvain Viguier, and Anne-Laure Ligozat. Estimating the carbon footprint of bloom, a 176b parameter language model. *Journal of Machine Learning Research*, 24(253):1–15, 2023.
- [12] Mark Horowitz. Computing’s energy problem (and what we can do about it). In *2014 IEEE international solid-state circuits conference digest of technical papers (ISSCC)*, pages 10–14. IEEE, 2014.
- [13] Yu-Hsin Chen, Joel Emer, and Vivienne Sze. Eyeriss: A spatial architecture for energy-efficient dataflow for convolutional neural networks. *ACM SIGARCH computer architecture news*, 44(3):367–379, 2016.
- [14] Alan Mathison Turing et al. On computable numbers, with an application to the entscheidungsproblem. *J. of Math*, 58(345-363):5, 1936.
- [15] John Von Neumann. First draft of a report on the edvac. Technical report, Moore School of Electrical Engineering, University of Pennsylvania, 1945.
- [16] Henry Markram, Eilif Muller, Srikanth Ramaswamy, Michael W Reimann, Marwan Abdellah, Carlos Aguado Sanchez, Anastasia Ailamaki, Lidia Alonso-Nanclares, Nicolas Antille, Selim Arsever, et al. Reconstruction and simulation of neocortical microcircuitry. *Cell*, 163(2):456–492, 2015.
- [17] Giacomo Indiveri and Shih-Chii Liu. Memory and information processing in neuromorphic systems. *Proceedings of the IEEE*, 103(8):1379–1397, 2015.
- [18] Paul A Merolla, John V Arthur, Rodrigo Alvarez-Icaza, Andrew S Cassidy, Jun Sawada, Philipp Akopyan, Bryan L Jackson, Nabil Imam, Chen Guo, Yutaka Nakamura, et al. A million spiking-neuron integrated circuit with a scalable communication network and interface. *Science*, 345(6197):668–673, 2014.

- [19] Daniel J Felleman and David C Van Essen. Distributed hierarchical processing in the primate cerebral cortex. *Cerebral cortex (New York, NY: 1991)*, 1(1):1–47, 1991.
- [20] André Moraes Bastos, Julien Vezoli, Conrado Arturo Bosman, Jan-Mathijs Schoffelen, Robert Oostenveld, Jarrod Robert Dowdall, Peter De Weerd, Henry Kennedy, and Pascal Fries. Visual areas exert feedforward and feedback influences through distinct frequency channels. *Neuron*, 85(2):390–401, 2015.
- [21] Stephen Grossberg. Competitive learning: From interactive activation to adaptive resonance. *Cognitive science*, 11(1):23–63, 1987.
- [22] Francis Crick. The recent excitement about neural networks. *Nature*, 337(6203):129–132, 1989.
- [23] Timothy P Lillicrap, Daniel Cownden, Douglas B Tweed, and Colin J Akerman. Random synaptic feedback weights support error backpropagation for deep learning. *Nature communications*, 7(1):13276, 2016.
- [24] Timothy P Lillicrap, Adam Santoro, Luke Marris, Colin J Akerman, and Geoffrey Hinton. Backpropagation and the brain. *Nature Reviews Neuroscience*, 21(6):335–346, 2020.
- [25] Blake A Richards and Timothy P Lillicrap. Dendritic solutions to the credit assignment problem. *Current opinion in neurobiology*, 54:28–36, 2019.
- [26] Sergey Bartunov, Adam Santoro, Blake Richards, Luke Marris, Geoffrey E Hinton, and Timothy Lillicrap. Assessing the scalability of biologically-motivated deep learning algorithms and architectures. *Advances in Neural Information Processing Systems*, 31, 2018.
- [27] Qianli Liao, Joel Leibo, and Tomaso Poggio. How important is weight symmetry in backpropagation? In *Proceedings of the AAAI Conference on Artificial Intelligence*, volume 30, 2016.
- [28] Will Xiao, Honglin Chen, Qianli Liao, and Tomaso Poggio. Biologically-plausible learning algorithms can scale to large datasets. In *International Conference on Learning Representations*, 2019.
- [29] James CR Whittington and Rafal Bogacz. An approximation of the error backpropagation algorithm in a predictive coding network with local hebbian synaptic plasticity. *Neural computation*, 29(5):1229–1262, 2017.
- [30] Yuhang Song, Beren Millidge, Tommaso Salvatori, Thomas Lukasiewicz, Zhenghua Xu, and Rafal Bogacz. Inferring neural activity before plasticity as a foundation for learning beyond backpropagation. *Nature Neuroscience*, 27(2):348–358, 2024.
- [31] Benjamin Scellier and Yoshua Bengio. Equilibrium propagation: Bridging the gap between energy-based models and backpropagation. *Frontiers in computational neuroscience*, 11:24, 2017.
- [32] John F Kolen and Jordan B Pollack. Backpropagation without weight transport. In *Proceedings of 1994 IEEE International Conference on Neural Networks (ICNN'94)*, volume 3, pages 1375–1380. IEEE, 1994.
- [33] Mohamed Akrouf, Collin Wilson, Peter Humphreys, Timothy Lillicrap, and Douglas B Tweed. Deep learning without weight transport. *Advances in Neural Information Processing Systems*, 32, 2019.
- [34] Lucia Galli and Lamberto Maffei. Spontaneous impulse activity of rat retinal ganglion cells in prenatal life. *Science*, 242(4875):90–91, 1988.
- [35] James B Ackman, Timothy J Burbridge, and Michael C Crair. Retinal waves coordinate patterned activity throughout the developing visual system. *Nature*, 490(7419):219–225, 2012.
- [36] Noelia Antón-Bolaños, Alejandro Sempere-Ferrández, Teresa Guillamón-Vivancos, Francisco J Martini, Leticia Pérez-Saiz, Henrik Gezelius, Anton Filipchuk, Miguel Valdeolmillos, and Guillermina López-Bendito. Prenatal activity from thalamic neurons governs the emergence of functional cortical maps in mice. *Science*, 364(6444):987–990, 2019.
- [37] Francisco J Martini, Teresa Guillamón-Vivancos, Verónica Moreno-Juan, Miguel Valdeolmillos, and Guillermina López-Bendito. Spontaneous activity in developing thalamic and cortical sensory networks. *Neuron*, 109(16):2519–2534, 2021.
- [38] Jeonghwan Cheon, Sang Wan Lee, and Se-Bum Paik. Pretraining with random noise for fast and robust learning without weight transport. In A. Globerson, L. Mackey, D. Belgrave, A. Fan, U. Paquet, J. Tomczak, and C. Zhang, editors, *Advances in Neural Information Processing Systems*, volume 37, pages 13748–13768. Curran Associates, Inc., 2024.

- [39] Yuval Netzer, Tao Wang, Adam Coates, Alessandro Bissacco, Baolin Wu, Andrew Y Ng, et al. Reading digits in natural images with unsupervised feature learning. In *NIPS workshop on deep learning and unsupervised feature learning*, number 2. Granada, 2011.
- [40] Alex Krizhevsky. Learning multiple layers of features from tiny images. Technical report, University of Toronto, 2009.
- [41] Adam Coates, Andrew Ng, and Honglak Lee. An analysis of single-layer networks in unsupervised feature learning. In *Proceedings of the fourteenth international conference on artificial intelligence and statistics*, pages 215–223. JMLR Workshop and Conference Proceedings, 2011.
- [42] Yann LeCun, Léon Bottou, Yoshua Bengio, and Patrick Haffner. Gradient-based learning applied to document recognition. *Proceedings of the IEEE*, 86(11):2278–2324, 1998.
- [43] Hao Li, Zheng Xu, Gavin Taylor, Christoph Studer, and Tom Goldstein. Visualizing the loss landscape of neural nets. In S. Bengio, H. Wallach, H. Larochelle, K. Grauman, N. Cesa-Bianchi, and R. Garnett, editors, *Advances in Neural Information Processing Systems*, volume 31. Curran Associates, Inc., 2018.
- [44] Zhewei Yao, Amir Gholami, Kurt Keutzer, and Michael W Mahoney. Pyhessian: Neural networks through the lens of the hessian. In *2020 IEEE international conference on big data (Big data)*, pages 581–590. IEEE, 2020.
- [45] Sepp Hochreiter and Jürgen Schmidhuber. Flat minima. *Neural computation*, 9(1):1–42, 1997.
- [46] Nitish Shirish Keskar, Dheevatsa Mudigere, Jorge Nocedal, Mikhail Smelyanskiy, and Ping Tak Peter Tang. On large-batch training for deep learning: Generalization gap and sharp minima. *arXiv preprint arXiv:1609.04836*, 2016.
- [47] Pratik Chaudhari, Anna Choromanska, Stefano Soatto, Yann LeCun, Carlo Baldassi, Christian Borgs, Jennifer Chayes, Levent Sagun, and Riccardo Zecchina. Entropy-sgd: Biasing gradient descent into wide valleys. *Journal of Statistical Mechanics: Theory and Experiment*, 2019(12):124018, 2019.
- [48] Pavel Izmailov, Dmitrii Podoprikin, Timur Garipov, Dmitry Vetrov, and Andrew Gordon Wilson. Averaging weights leads to wider optima and better generalization. *arXiv preprint arXiv:1803.05407*, 2018.
- [49] Pierre Foret, Ariel Kleiner, Hossein Mobahi, and Behnam Neyshabur. Sharpness-aware minimization for efficiently improving generalization. In *International Conference on Learning Representations*, 2021.
- [50] Dan Hendrycks and Thomas Dietterich. Benchmarking neural network robustness to common corruptions and perturbations. In *International Conference on Learning Representations*, 2019.
- [51] Ian J Goodfellow, Jonathon Shlens, and Christian Szegedy. Explaining and harnessing adversarial examples. *arXiv preprint arXiv:1412.6572*, 2014.
- [52] Xavier Glorot and Yoshua Bengio. Understanding the difficulty of training deep feedforward neural networks. In *Proceedings of the thirteenth international conference on artificial intelligence and statistics*, pages 249–256. JMLR Workshop and Conference Proceedings, 2010.
- [53] Ilya Sutskever, James Martens, George Dahl, and Geoffrey Hinton. On the importance of initialization and momentum in deep learning. In *International conference on machine learning*, pages 1139–1147. PMLR, 2013.
- [54] Kaiming He, Xiangyu Zhang, Shaoqing Ren, and Jian Sun. Delving deep into rectifiers: Surpassing human-level performance on imagenet classification. In *Proceedings of the IEEE international conference on computer vision*, pages 1026–1034, 2015.
- [55] Andrew M Saxe, James L McClelland, and Surya Ganguli. Exact solutions to the nonlinear dynamics of learning in deep linear neural networks. *arXiv preprint arXiv:1312.6120*, 2013.
- [56] Jeonghwan Cheon and Se-Bum Paik. Pretraining with random noise for uncertainty calibration. *arXiv preprint arXiv:2412.17411*, 2024.
- [57] Logan G Wright, Tatsuhiro Onodera, Martin M Stein, Tianyu Wang, Darren T Schachter, Zoey Hu, and Peter L McMahon. Deep physical neural networks trained with backpropagation. *Nature*, 601(7894):549–555, 2022.
- [58] Ali Momeni, Babak Rahmani, Matthieu Malléjac, Philipp Del Hougne, and Romain Fleury. Backpropagation-free training of deep physical neural networks. *Science*, 382(6676):1297–1303, 2023.

- [59] Alexey Kurakin, Ian J Goodfellow, and Samy Bengio. Adversarial examples in the physical world. In *Artificial intelligence safety and security*, pages 99–112. Chapman and Hall/CRC, 2018.
- [60] Aleksander Madry, Aleksandar Makelov, Ludwig Schmidt, Dimitris Tsipras, and Adrian Vladu. Towards deep learning models resistant to adversarial attacks. *arXiv preprint arXiv:1706.06083*, 2017.
- [61] Zhewei Yao, Amir Gholami, Qi Lei, Kurt Keutzer, and Michael W Mahoney. Hessian-based analysis of large batch training and robustness to adversaries. In S. Bengio, H. Wallach, H. Larochelle, K. Grauman, N. Cesa-Bianchi, and R. Garnett, editors, *Advances in Neural Information Processing Systems*, volume 31. Curran Associates, Inc., 2018.
- [62] Haim Avron and Sivan Toledo. Randomized algorithms for estimating the trace of an implicit symmetric positive semi-definite matrix. *Journal of the ACM (JACM)*, 58(2):1–34, 2011.
- [63] Gene H Golub and John H Welsch. Calculation of gauss quadrature rules. *Mathematics of computation*, 23(106):221–230, 1969.
- [64] Behrooz Ghorbani, Shankar Krishnan, and Ying Xiao. An investigation into neural net optimization via hessian eigenvalue density. In Kamalika Chaudhuri and Ruslan Salakhutdinov, editors, *Proceedings of the 36th International Conference on Machine Learning*, volume 97 of *Proceedings of Machine Learning Research*, pages 2232–2241. PMLR, 09–15 Jun 2019.

A Supplementary results

A.1 One-time initial alignment enables learning without weight transport

A.1.1 Layer-wise weight alignment dynamics

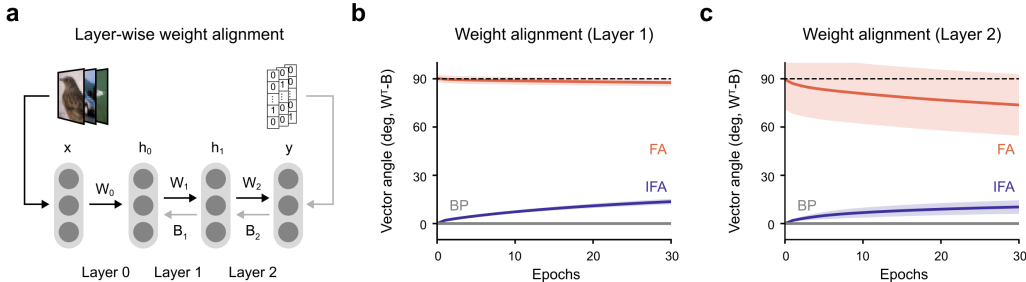


Figure S1: Weight alignment between forward and backward weights during learning. (a) Schematic of the three-layer feedforward neural network and its learning process. Forward and backward weights are analyzed in all layers except the first (Layer 0). (b-c) Alignment angle between forward and backward weights in each layer of the network. (b) Weight alignment in Layer 1. The shaded area represents the standard deviation of alignment angles across 512 neurons. (c) Weight alignment in Layer 2, the final layer of the network. The shaded area represents the standard deviation of alignment angles across 512 neurons.

To generalize the trend of alignment dynamics observed in the penultimate layer (Figure 1f), we extended the analysis to all layers (Figure S1a). With the exception of the first layer, which lacks corresponding backward weights, we examined the vector angles between forward and backward weights in the second (Figure S1b) and final layers (Figure S1c). Consistent with the main results, feedback alignment (FA) [23] learns by aligning forward weights with backward weights over the course of training, whereas standard backpropagation (BP) [1] enforces identical forward and backward weights. Our model, initial feedback alignment (IFA), learns by gradually relaxing this alignment during training.

A.1.2 Training details for different learning models

To investigate the impact of initial alignment on neural network learning, we visualized learning curves under three different learning rules: (1) BP, (2) FA, and (3) IFA, while keeping all other experimental conditions constant. We plotted training accuracy (Figure S2a), training loss (Figure S2b), test accuracy (Figure S2c), and test loss (Figure S2d) over the course of training. Baseline FA exhibited slower convergence and lower performance compared to standard BP. In contrast, IFA achieved comparable learning speed and accuracy to BP, with nearly overlapping learning curves for both the training and test sets.

A.1.3 Validation across neural network architectures

Table S1: Benchmarked performance of the convolutional neural networks. Each performance value (%) is reported as the mean \pm standard deviation across ten independent trials.

		2 Conv + 3 FC	5 Conv + 3 FC
	BP	62.13 \pm 0.90	73.10 \pm 0.29
FA	90°	45.67 \pm 1.71	50.41 \pm 1.11
IFA	0°	56.37 \pm 1.24	65.55 \pm 0.62

Our main results, obtained using multi-layer feedforward neural networks, demonstrated that initial alignment enhances the scalability of feedback alignment algorithms. To assess whether this effect generalizes to other architectures and deeper models, we further evaluated convolutional neural networks (CNNs) (Figure S3). We first tested a LeNet-variant CNN [42] with two convolutional

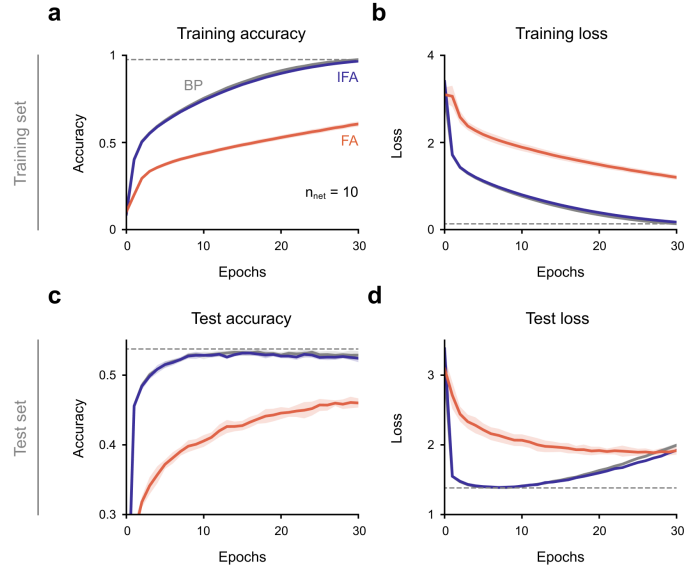


Figure S2: Learning curves across different feedback dynamics. (a–d) Learning curves over the course of training. (a) Training accuracy. (b) Training loss. (c) Test accuracy. (d) Test loss. The dotted gray horizontal line represents the final performance achieved by BP. The shaded area denotes the standard deviation across ten independent trials.

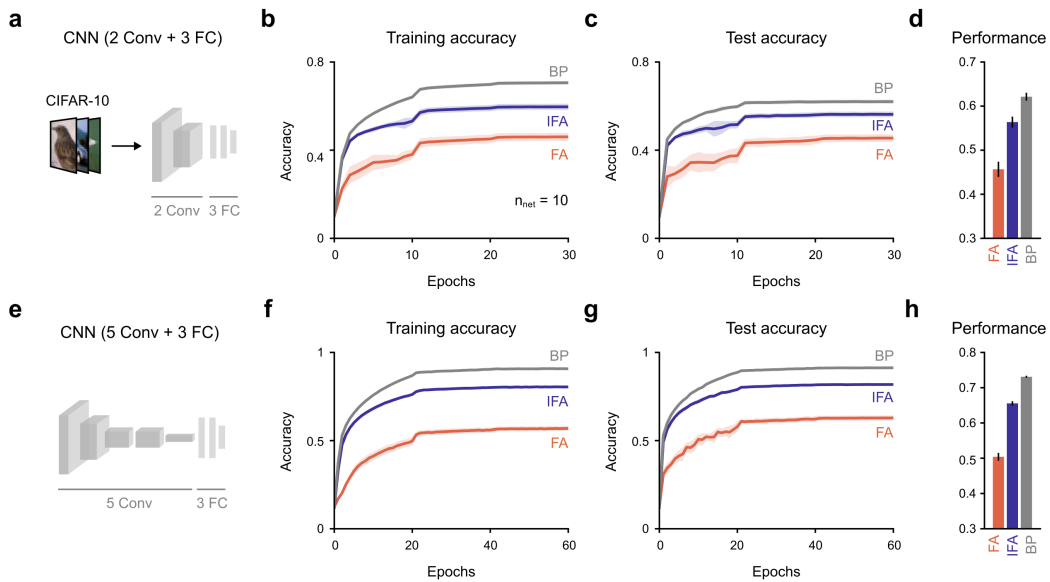


Figure S3: Effect of initial weight alignment on convolutional neural networks. (a) A convolutional neural network variant of LeNet, consisting of two convolutional layers and three fully connected layers, is used. The model is trained on CIFAR-10. (b) Training accuracy. (c) Test accuracy. (d) Final test accuracy. (e) A convolutional neural network variant of AlexNet, consisting of five convolutional layers and three fully connected layers, is used. (f) Training accuracy. (g) Test accuracy. (h) Final test accuracy. The shaded areas in the line plots and the error bars in the bar plots represent the standard deviation across ten independent trials.

layers and three fully connected layers (Figure S3a). We found that both the training and test accuracy of IFA were significantly higher than those of baseline FA, and the performance gap between IFA and BP was reduced (Figure S3b, c). The final test performance of IFA substantially outperformed that of

baseline FA (Figure S3d; Table S1). We also evaluated an AlexNet-variant CNN [3] consisting of five convolutional layers and three fully connected layers (Figure S3e), and observed a similar trend (Figure S3f–h; Table S1). For training, we used the Adam optimizer with learning rates of 0.001 and 0.0001, and applied weight decay with a decay coefficient of 0.0001 to prevent overfitting. These findings suggest that IFA is broadly applicable to neural architectures beyond multi-layer perceptrons and can scale effectively to modern deep learning models.

A.1.4 Benchmarking model performance on standard datasets

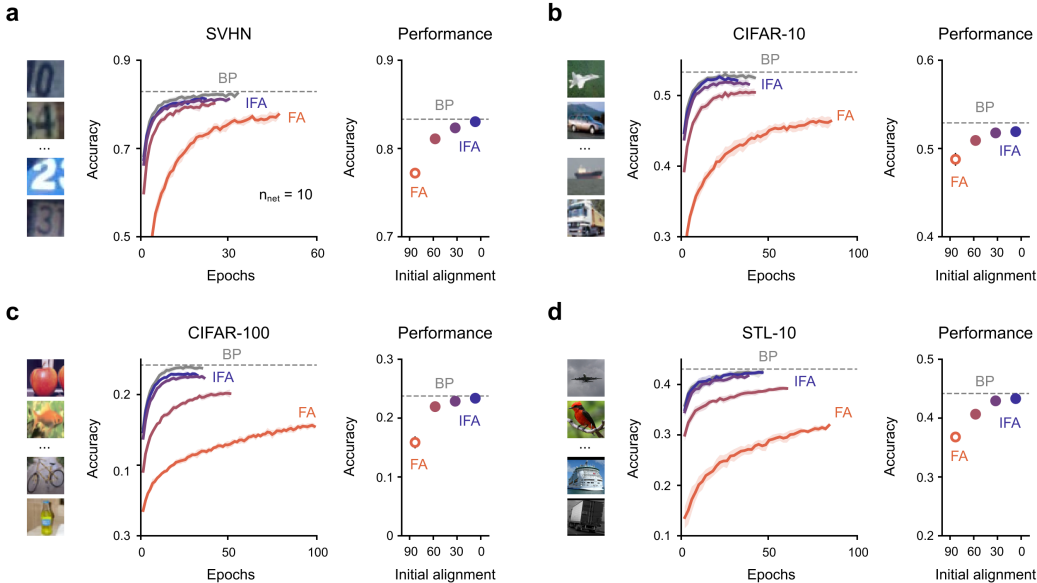


Figure S4: Benchmarked network performance across various image datasets. (a–d) Learning curves showing test accuracy over the course of training (left) and the benchmarked final test accuracy (right). (a) SVHN. (b) CIFAR-10. (c) CIFAR-100. (d) STL-10.

Table S2: Performance of the model on each dataset (SVHN, CIFAR-10, CIFAR-100, STL-10). Each performance value (%) is reported as the mean \pm standard deviation across ten independent trials.

	SVHN	CIFAR-10	CIFAR-100	STL-10
BP	82.90 \pm 0.11	53.32 \pm 0.27	24.18 \pm 0.28	43.75 \pm 0.22
FA	90° 78.78 \pm 0.72	47.21 \pm 0.35	16.79 \pm 0.57	35.87 \pm 1.01
	60° 80.91 \pm 0.16	51.09 \pm 0.43	20.66 \pm 0.36	41.95 \pm 0.24
IFA	30° 81.76 \pm 0.16	52.33 \pm 0.30	22.93 \pm 0.12	42.87 \pm 0.30
	0° 81.91 \pm 0.20	53.04 \pm 0.33	23.31 \pm 0.20	43.37 \pm 0.31

Our main results were obtained using the CIFAR-10 dataset. To demonstrate that IFA generalizes across various datasets, we benchmarked the performance of BP, FA, and IFA on SVHN [39] (Figure S4a), CIFAR-10 [40] (Figure S4b), CIFAR-100 [40] (Figure S4c), and STL-10 [41] (Figure S4d). Final accuracy was evaluated by extending training until test accuracy stopped improving for ten consecutive epochs (Table S2). Consistent with our main findings, the performance of baseline FA was significantly lower than that of BP. However, incorporating initial alignment substantially improved performance, in some cases reaching levels comparable to backpropagation. These results suggest that IFA is generalizable across different datasets and can effectively enhance learning performance.

A.2 Stabilizing learning through initial weight alignment

A.2.1 Training networks across the parameter space

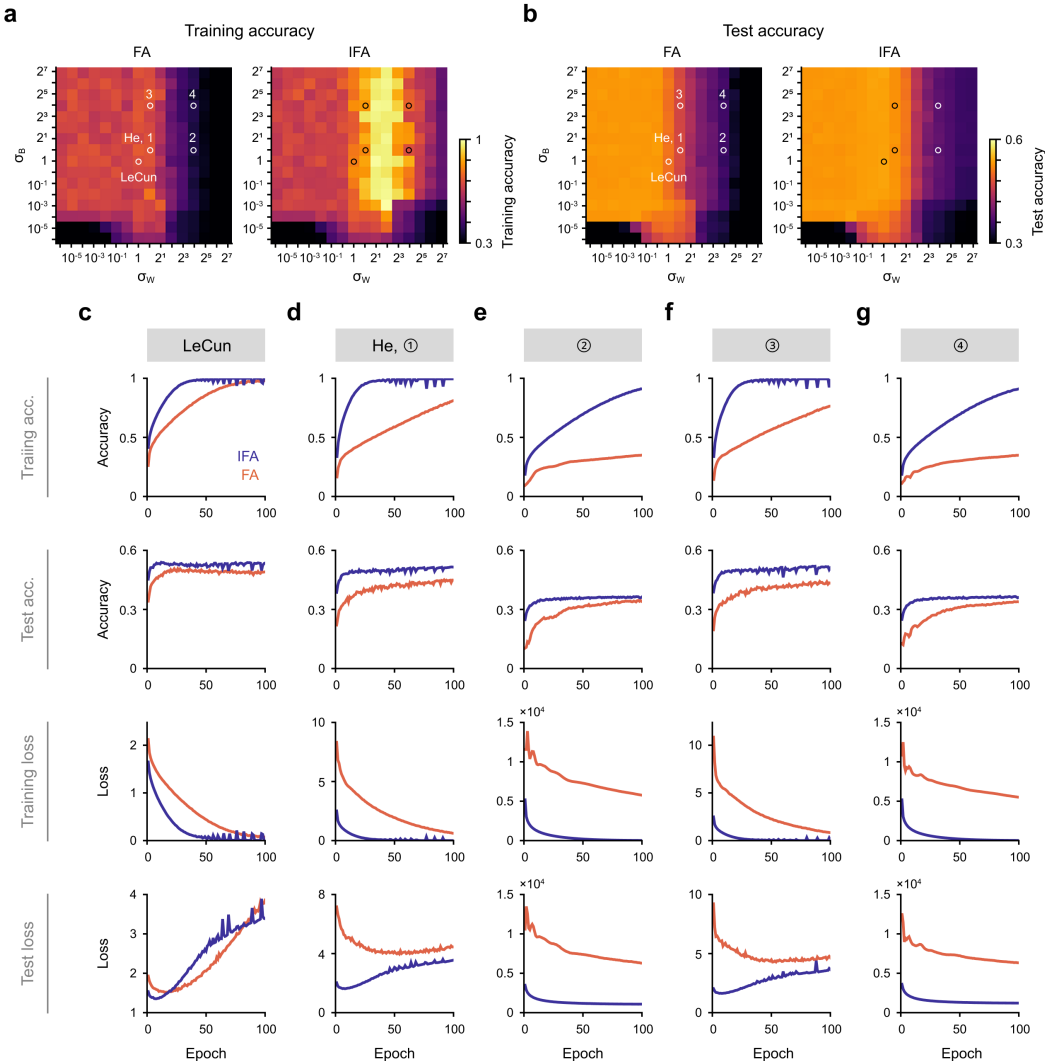


Figure S5: Trainability and generalization across the parameter space. (a) Training accuracy across the parameter space, with color indicating the final training accuracy. (b) Test accuracy across the parameter space, with color indicating the final test accuracy. The x- and y-axes represent the variances of the forward and backward weights, respectively. The point $(1, 1)$ corresponds to LeCun initialization (c), and $(\sqrt{2}, \sqrt{2})$ corresponds to He initialization (d; ①). Additionally, we investigate several representative conditions to visualize learning curves: large forward weight variance at $(2^4, \sqrt{2})$ (e; ②), large backward weight variance at $(\sqrt{2}, 2^4)$ (f; ③), and large variance in both weights at $(2^4, 2^4)$ (g; ④). For each variance condition, learning curves of training accuracy, test accuracy, training loss, and test loss are presented from top to bottom.

In the main results, we reported the trainability of networks using FA and IFA across a parameter space defined by a two-dimensional grid of varying forward and backward weight variances (Figure 3a; Figure S5a). We observed that baseline FA supports only a narrow range of variance settings for achieving high training accuracy, whereas IFA enables a broader trainable parameter space. To extend this analysis, we also evaluated generalization by measuring test accuracy across the same parameter space (Figure S5b). Consistent with the trainability results, we found that initial alignment

significantly expands the range of variance settings that yield high test accuracy. Furthermore, IFA consistently outperformed FA in nearly all regions of the parameter space.

To further characterize the learning behavior of FA and IFA, we selected five representative parameter settings and visualized the corresponding learning curves (Figure S5c–g). We first examined standard initialization methods: LeCun initialization (Figure S5c, (1, 1)) and He initialization (Figure S5d, $(\sqrt{2}, \sqrt{2})$, ①), confirming that IFA achieves faster convergence and higher performance in both training and test accuracy. We then extended the analysis to more extreme conditions, including large forward weight variance (Figure S5e, $(2^4, \sqrt{2})$, ②), large backward weight variance (Figure S5f, $(\sqrt{2}, 2^4)$, ③), and large variance in both forward and backward weights (Figure S5g, $(2^4, 2^4)$, ④). While FA exhibited extreme instability under these conditions, IFA demonstrated robust learning dynamics, with improved trainability and generalization.

A.2.2 Training networks with varying depth

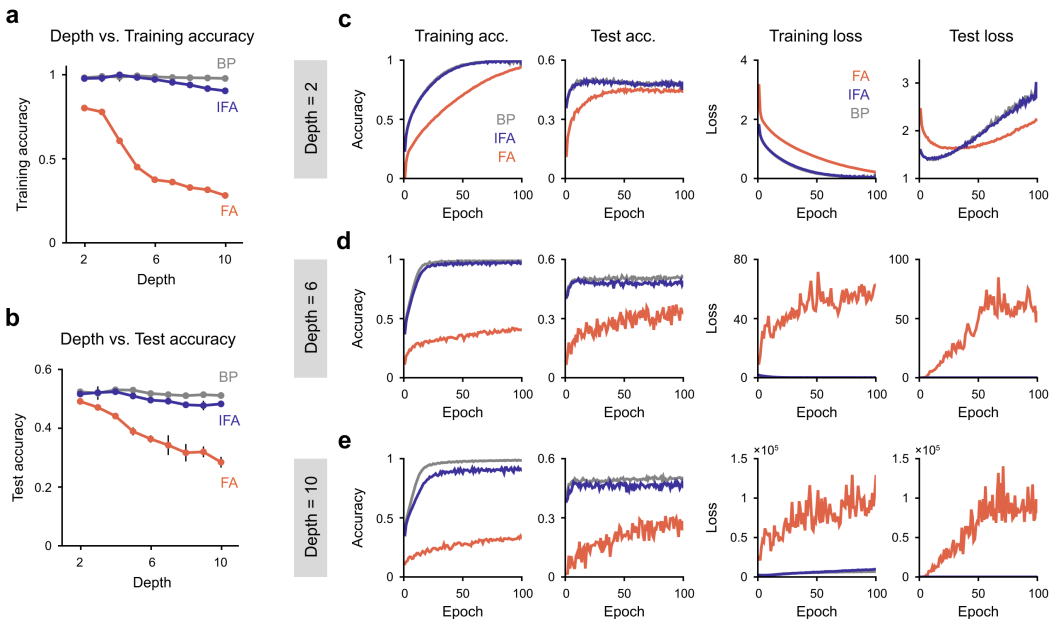


Figure S6: Trainability and generalization across different network depths. (a) Training accuracy as a function of network depth, for feedforward networks with depths ranging from 2 to 10 layers. (b) Test accuracy as a function of network depth, using the same range. (c-e) Learning curves for representative depths: 2 (c), 6 (d), and 10 (e). For each depth, training accuracy, test accuracy, training loss, and test loss are shown from left to right.

We also extended our trainability analysis to networks with varying depths (Figure 3b; Figure S6a) and benchmarked test accuracy to assess generalization performance (Figure S6b). Consistent with the trainability results, IFA achieved significantly higher test accuracy than baseline FA and performed comparably to BP. Notably, FA exhibited a steep decline in test performance as network depth increased, whereas IFA maintained high test accuracy even in deeper architectures. To further investigate this trend, we selected three representative network depths and visualized the corresponding learning curves: depth 2 (Figure S6c), depth 6 (Figure S6d), and depth 10 (Figure S6e). As depth increased, baseline FA showed highly unstable learning dynamics — loss values diverged, and accuracy fluctuated significantly. In contrast, IFA demonstrated robust and stable learning, closely matching the behavior of standard BP. Interestingly, in deeper networks, FA’s loss continued to increase even as accuracy slightly improved. This discrepancy between loss and accuracy suggests a breakdown in model calibration: the network’s confidence estimates become misaligned with actual prediction performance.

A.2.3 Training with limited data

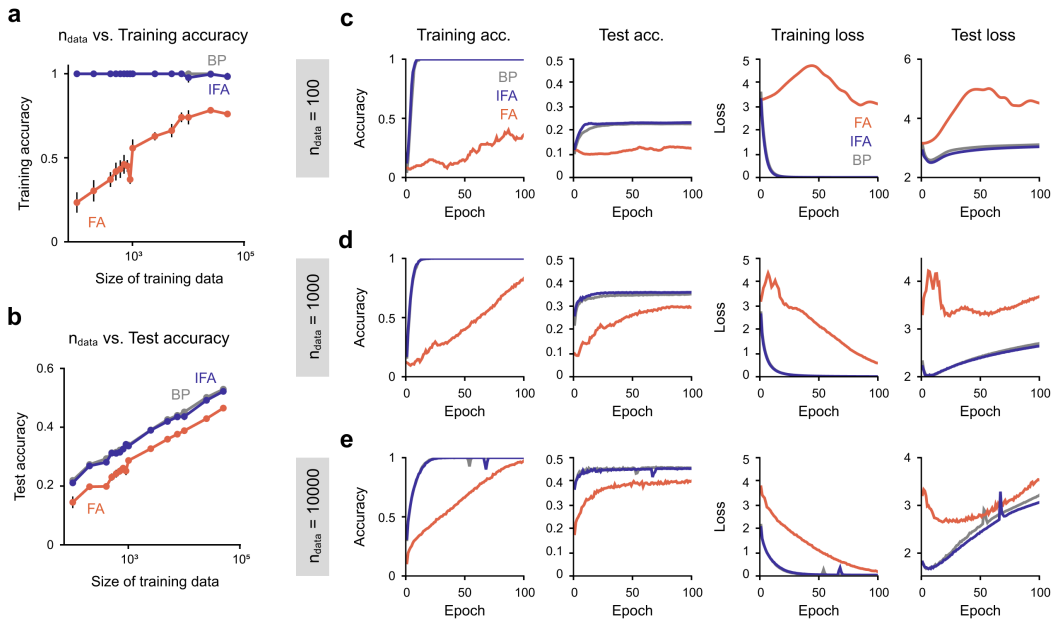


Figure S7: Trainability and generalization under limited data. (a) Training accuracy as a function of training data size, for feedforward networks trained on datasets ranging from 100 to 50,000 samples. (b) Test accuracy as a function of training data size, using the same range. (c-e) Learning curves for representative data sizes: 100 samples (c), 1,000 samples (d), and 10,000 samples (e). For each data size, training accuracy, test accuracy, training loss, and test loss are shown from left to right.

Next, we investigated the effect of limited training data size (Figure 3c; Figure S7a) on generalization performance (Figure S7b). We benchmarked the test accuracy of networks trained on varying amounts of data. Notably, baseline FA consistently exhibited poor test performance compared to BP when trained on the same number of samples. In contrast, IFA demonstrated substantially improved generalization over FA, often achieving performance levels close to those of BP. The relationship between dataset size and test accuracy is frequently discussed in the context of neural scaling laws. Within this framework, initial alignment effectively shifts the scaling curve upward, enabling improved performance at every dataset size. To further examine this behavior, we selected three representative training data conditions and visualized the corresponding learning curves: 100 samples (Figure S7c), 1,000 samples (Figure S7d), and 10,000 samples (Figure S7e). Baseline FA notably struggled to learn under limited data, likely due to its reliance on data-driven alignment over time. In contrast, IFA produced stable and effective learning dynamics, even in data-scarce regimes.

A.3 Initial alignment enhances robust generalization

A.3.1 Layer-wise dynamics of weight alignment

In the main results (Figure 4b), we visualized the alignment dynamics in the penultimate layer under various initial alignment conditions. We further extended this analysis to all layers (Figure S8a). With the exception of the first layer, we examined the angle between forward and backward weight vectors in both the second layer (Figure S1b) and the final layer (Figure S1c). Consistent with our main findings, the learning dynamics were highly dependent on the initial alignment. When the initial alignment was strong, the network gradually decreased the alignment during training. In contrast, when the initial alignment was weak, the network progressively increased the alignment through learning.

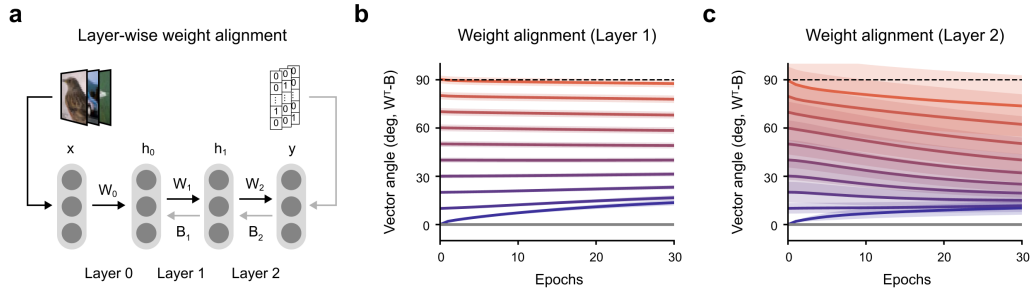


Figure S8: Effect of initial weight alignment on alignment dynamics during learning. (a) Schematic of a three-layer feedforward neural network. Forward and backward weights, excluding those in the first layer (Layer 0), are initialized with a soft alignment, ranging from 0° to 90° . An initial angle of 90° corresponds to the baseline feedback alignment. (b–c) Alignment angles between forward and backward weights in each layer. (b) Weight alignment in Layer 1. Shaded areas indicate the standard deviation of alignment angles across 512 neurons. (c) Weight alignment in Layer 2, the final layer of the network. Shaded areas indicate the standard deviation of alignment angles across 512 neurons.

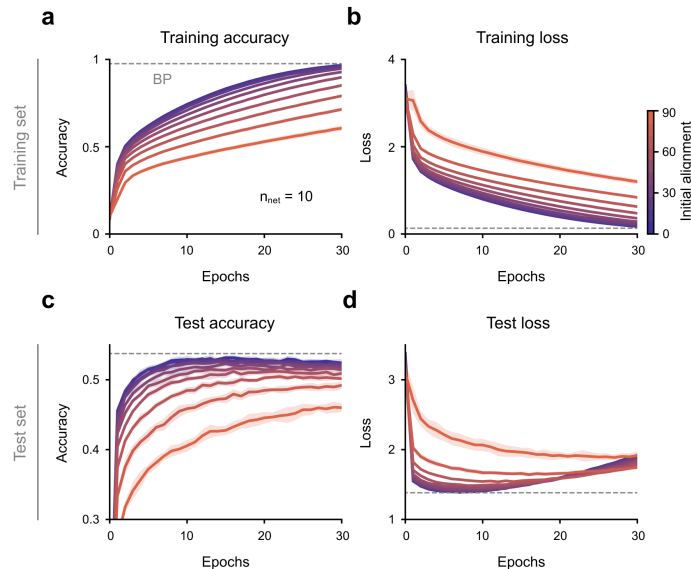


Figure S9: Learning curves across various initial alignment angles. (a–d) Learning curves over the course of training. (a) Training accuracy. (b) Training loss. (c) Test accuracy. (d) Test loss. The dotted gray horizontal line indicates the final performance of BP. Each solid line represents the learning curve of networks with a different initial alignment angle. Shaded areas indicate the standard deviation across ten independent trials.

A.3.2 Training details for different learning models

Next, we examined how initial alignment influences neural network learning. To isolate its effect, we visualized learning curves across a range of initial alignment angles while keeping all other experimental conditions constant. Specifically, we plotted training accuracy (Figure S9a), training loss (Figure S9b), test accuracy (Figure S9c), and test loss (Figure S9d) over the course of training. Our results show that although baseline FA performs poorly compared to BP, increasing the initial alignment markedly improves both learning speed and performance. As the alignment increases, the learning curves progressively resemble those of standard BP.

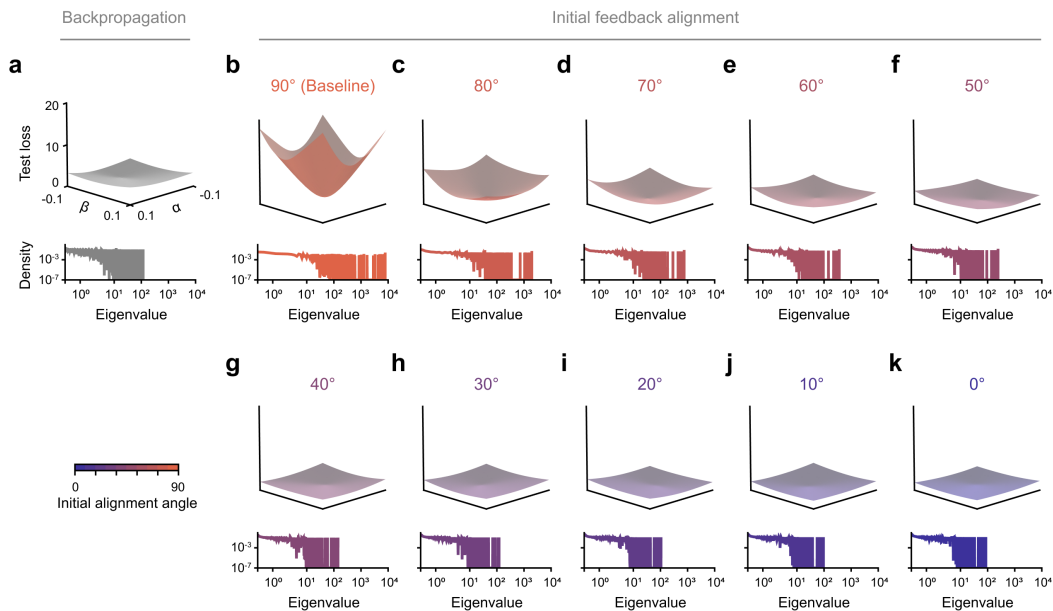


Figure S10: Spectral analysis of convergence behavior across initial alignment angles. (a–k) Loss landscapes visualized by perturbing the trained model parameters within a two-dimensional subspace defined by the top two eigenvectors of the Hessian (top). The axes, denoted by α and β , correspond to scaling factors for perturbations along the first and second eigenvector directions, respectively. Below each landscape, the spectral density of the Hessian eigenvalues is shown (bottom). (a) BP. (b–k) IFA with varying initial alignment angles ranging from 0° to 90° . An initial angle of 90° (b) corresponds to the baseline feedback alignment.

A.3.3 Extended spectral analysis

To further investigate how initial weight alignment influences the convergence behavior of neural networks, we conducted a spectral analysis of the loss landscape (Figure S10). For each trained model, we visualized the local geometry of the loss surface by perturbing the parameters within a two-dimensional subspace spanned by the top two eigenvectors of the Hessian matrix. Specifically, we plotted the loss as a function of perturbations along these principal curvature directions, denoted by α and β , to assess the flatness and sharpness of the local minima. In addition, we examined the Hessian spectrum by plotting the eigenvalue density distribution. We first observed that BP exhibits a relatively flat loss landscape and a narrow eigenvalue spectrum (Figure S10a), in contrast to baseline FA, which shows a sharper landscape and a broader spectrum (Figure S10b). However, as the initial alignment improved (i.e., as the alignment angle decreased), the loss landscape became progressively flatter, and the Hessian spectra became increasingly concentrated within a narrower range (Figures S10c–k). These findings suggest that stronger initial alignment leads to smoother loss surfaces and more favorable curvature properties, ultimately enhancing robustness and generalization.

A.3.4 Robustness under input corruption

To further assess the impact of initial weight alignment on model robustness, we systematically evaluated performance under varying levels of input corruption (Figure S11). Following a standard image corruption benchmark [50], we applied fifteen corruption types—categorized into noise, blur, weather, and digital—to the test set, each at five severity levels ranging from level 1 (least severe) to level 5 (most severe) (Figure S11a). While results for severity level 1 were presented in the main text (Figure 6b, c), here we report extended results for severity levels 2 through 5 (Figures S11b–e). We compared the corruption robustness of networks initialized with different alignment conditions by measuring their classification accuracy on both clean and corrupted inputs. Consistent with our main results, FA showed substantially lower robustness compared to standard BP. However, increasing the degree of initial alignment significantly improved robustness, bringing performance closer to that of BP. Although all models exhibited performance degradation as corruption severity increased,

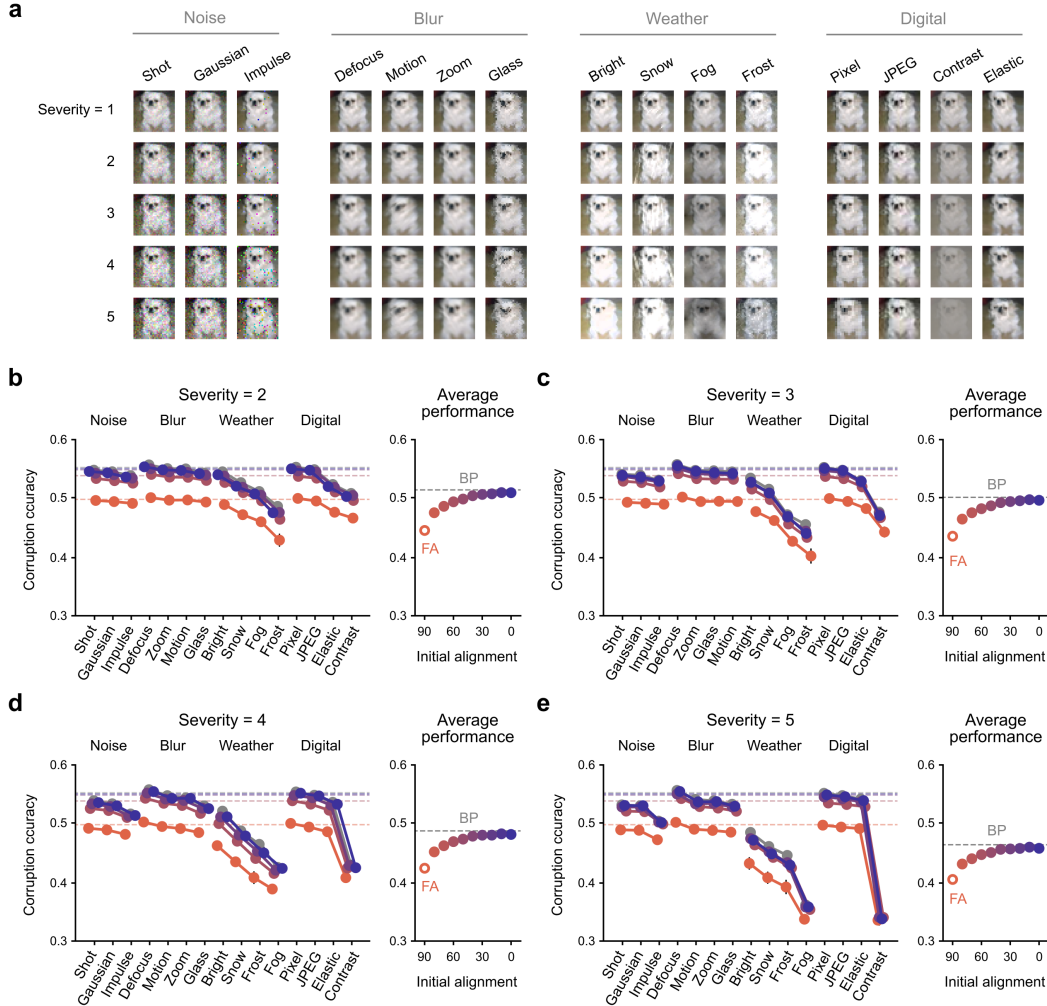


Figure S11: Effect of initial weight alignment on robustness to input corruption of varying severity. (a) Fifteen image corruption types, grouped into four categories—noise, blur, weather, and digital—were applied to test samples to assess network robustness. Each corruption type was tested across five severity levels, ranging from 1 (least severe) to 5 (most severe). (b–f) Classification accuracy on corrupted inputs (solid lines with markers) compared to accuracy on clean, uncorrupted images (dotted lines) (left). The relationship between initial alignment angle and robustness, measured as the average accuracy across all corruption types, is shown on the right. (b) Severity 2 (Severity 1 is shown in the main results). (c) Severity 3. (d) Severity 4. (e) Severity 5.

the decline was significantly less pronounced in networks with stronger initial alignment. These results highlight the robustness benefits conferred by initial alignment—networks with better-aligned initial weights demonstrated greater resilience to input corruptions, suggesting that alignment at initialization helps stabilize learning and supports more reliable performance under distributional shifts. This observation aligns with our earlier spectral analysis of the loss landscape, which showed that stronger initial alignment leads to flatter optima.

A.4 The role of weight misalignment in promoting adversarial robustness

A.4.1 Adversarial robustness to Basic Iterative Method (BIM)

In the main results, we demonstrated that the misalignment introduced by IFA enhances robustness against adversarial attacks, particularly using the Fast Gradient Sign Method (FGSM) (Figure 7). To further support this finding and extend the robustness of IFA to other gradient-based attacks, we also

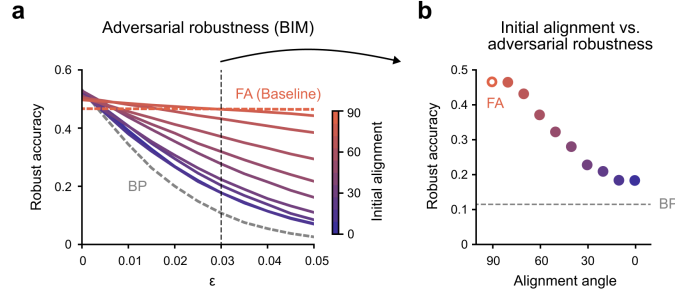


Figure S12: Effect of weight misalignment on adversarial robustness to the Basic Iterative Method (BIM). (a) Classification accuracy as a function of increasing adversarial perturbation strength under attack using the BIM. (b) Relationship between the initial alignment angle and adversarial robustness, measured as classification accuracy under attack with perturbation magnitude $\epsilon = 0.03$.

evaluated performance under the Basic Iterative Method (BIM) [59]. BIM is an extension of FGSM that applies small, iterative perturbations in the direction of the gradient of the loss with respect to the input. At each step, the perturbation is constrained within a defined epsilon-ball around the original input to preserve perceptual similarity. We applied BIM to networks trained with various initial alignment angles and measured classification accuracy under increasing adversarial perturbation (Figure S12a). Consistent with our FGSM results, model accuracy under BP rapidly declined as perturbation strength increased, whereas models trained with IFA maintained significantly higher accuracy even under stronger attacks (Figure S12b).

A.4.2 Adversarial robustness to Projected Gradient Descent (PGD)

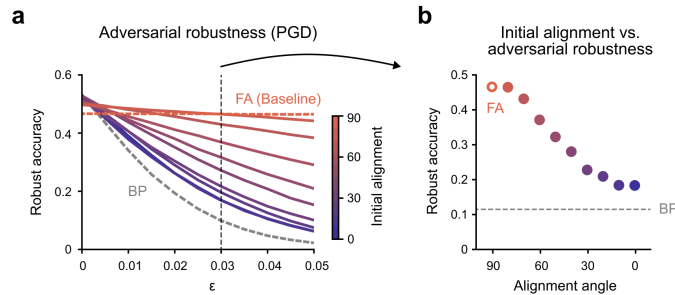


Figure S13: Effect of weight misalignment on adversarial robustness to the Projected Gradient Descent (PGD). (a) Classification accuracy as a function of increasing adversarial perturbation strength under attack using the PGD. (b) Relationship between the initial alignment angle and adversarial robustness, measured as classification accuracy under attack with perturbation magnitude $\epsilon = 0.03$.

We also evaluated robustness against the Projected Gradient Descent (PGD) attack [60], widely considered one of the most effective first-order adversarial attacks. PGD is an iterative extension of the Basic Iterative Method (BIM) that incorporates a projection step to ensure that adversarial examples remain within an ϵ -bounded ℓ_∞ -ball around the original input. At each iteration, the input is updated by ascending the gradient of the loss with respect to the input, followed by a projection back into the allowed perturbation region if the update exceeds the specified bound. We applied PGD to networks with varying initial alignment angles and measured their accuracy under attack (Figure S13a). Consistent with the results from FGSM and BIM, IFA-trained models showed significantly greater resilience to PGD compared to those trained with standard BP (Figure S13b). These findings reinforce the role of initial alignment in enhancing both generalization and robustness to strong adversarial attacks. In particular, they suggest that greater initial misalignment further improves adversarial robustness, highlighting a key functional advantage of IFA over standard BP.

B Methods

B.1 Neural network models

We employed a multi-layer feedforward neural network f_θ for image classification throughout the research. Specifically, the network begins with an input layer that receives a flattened one-dimensional vector of the input image. It then processes the input through multiple hidden, fully connected layers with forward weights $\mathbf{W}_l \in \mathbb{R}^{m \times n}$ and biases $\mathbf{b}_l \in \mathbb{R}^n$. Each hidden layer applies a nonlinear activation function to its output. We used two hidden layers, each with 512 units, and employed the Rectified Linear Unit (ReLU) as the activation function. The final layer applies a SoftMax function to produce a probability distribution over image categories. The forward weights \mathbf{W}_l were initialized using a normal distribution with zero mean and a standard deviation scaled according to the input size. Unlike standard backpropagation (BP), which uses the transpose of the forward weights for error propagation, feedback alignment (FA) utilizes separate backward weights $\mathbf{B}_l \in \mathbb{R}^{n \times m}$. These backward weights \mathbf{B}_l are also initialized randomly from the same distribution as the corresponding forward weights but remain fixed during training.

B.2 Soft Initial Alignment

In baseline Feedback Alignment (FA), the forward weights \mathbf{W}_l and backward weights \mathbf{B}_l are initialized independently using random distributions. In contrast, our proposed method—initial feedback alignment (IFA)—introduces a soft alignment at initialization, wherein the forward weights are sampled from a subspace partially aligned with the backward weights. Specifically, the forward weights \mathbf{W}_l are initialized by projecting onto a subspace spanned by the backward weights \mathbf{B}_l^\top and an independent random matrix \mathbf{R} :

$$\mathbf{B}_l \sim \mathcal{N}\left(0, \frac{a^2}{fan_{in}}\right), \quad \mathbf{R} \sim \mathcal{N}\left(0, \frac{a^2}{fan_{in}}\right)$$
$$\mathbf{W}_l = \mathbf{B}_l^\top \cos(\theta_{init}) + \mathbf{R} \sin(\theta_{init}),$$

where fan_{in} denotes the number of input units to the layer, and $a = \sqrt{2}$ follows the He initialization scheme, which is suitable for networks using ReLU activations. This initialization forms a linear combination of aligned and random components, with the parameter θ_{init} controlling the degree of initial alignment. When $\theta_{init} = 0^\circ$, the forward and backward weights are fully aligned ($\mathbf{W}_l = \mathbf{B}_l^\top$), whereas $\theta_{init} = 90^\circ$ corresponds to the standard FA case, where \mathbf{W}_l and \mathbf{B}_l^\top are orthogonal and thus unaligned.

B.3 Neural networks training

To evaluate the effects of different feedback dynamics, we trained neural networks using three distinct learning rules that differ only in how feedback signals are computed: (1) standard backpropagation (BP), (2) feedback alignment (FA), and (3) initial feedback alignment (IFA). Except for the feedback pathway, all other training conditions were held constant to ensure a fair comparison across methods. We employed the Adam optimizer with hyperparameters $\beta_1 = 0.99$, $\beta_2 = 0.999$, and a fixed learning rate of 10^{-4} . The training was performed using a batch size of 128 for 30 epochs in the main experiments, with extended training conducted for benchmarking or additional analyses when necessary. The primary dataset used was CIFAR-10, which comprises 50,000 training images and 10,000 test images. To assess generalizability, we also evaluated our methods on the CIFAR-100 and STL-10 datasets; these results are reported in the Supplementary Results.

B.4 Measurement of the alignment between forward and backward weights

To quantitatively assess the alignment between the forward weights $\mathbf{W}_l \in \mathbb{R}^{m \times n}$ and the backward weights $\mathbf{B}_l \in \mathbb{R}^{n \times m}$ at layer l , we computed the angular similarity between corresponding forward and backward weight vectors. For the i -th neuron in layer l , the forward weight vector is defined as the i -th row of \mathbf{W}_l^\top , denoted $\mathbf{W}_l^{\top(i)} \in \mathbb{R}^n$, and the corresponding backward weight vector is the i -th row of \mathbf{B}_l , denoted $\mathbf{B}_l^{(i)} \in \mathbb{R}^n$. The alignment angle between the two vectors was then computed using the cosine similarity [23]:

$$\theta_i = \cos^{-1} \left(\frac{\mathbf{W}_l^{\top (i)} \cdot \mathbf{B}_l^{(i)}}{\|\mathbf{W}_l^{\top (i)}\| \|\mathbf{B}_l^{(i)}\|} \right),$$

where θ_i represents the alignment angle for the i -th neuron. A smaller angle (closer to 0°) indicates stronger alignment between the forward and backward weights, whereas a larger angle (closer to 90°) indicates weaker or no alignment. We reported the average alignment across all neurons as a summary metric of the overall correspondence between the forward and backward pathways in the network.

B.5 Trainability analysis

To evaluate whether neural networks remain trainable under different feedback dynamics, we assessed trainability by benchmarking accuracy with various conditions. Specifically, we trained neural network models for 100 epochs and recorded the maximum training accuracy achieved. We examined the effects of several conditions on trainability: (1) variance of forward and backward weights, (2) network depth, and (3) size of the training dataset. While our primary focus was on training accuracy as a measure of trainability, we also reported test accuracy in the Supplementary Results.

First, we evaluated the trainable parameter space by systematically varying the variances of the forward and backward weights. Networks were initialized using zero-mean normal distributions with different variances:

$$\mathbf{W}_l \sim \mathcal{N} \left(0, \frac{a^2}{fan_{in}} \right), \quad \mathbf{B}_l \sim \mathcal{N} \left(0, \frac{b^2}{fan_{in}} \right),$$

where fan_{in} denotes the number of input units to each layer, and a and b are scaling parameters controlling the variance. Biases were initialized to zero. For example, $(a, b) = (1, 1)$ corresponds to LeCun initialization, and $(\sqrt{2}, \sqrt{2})$ corresponds to He initialization. We also explored a wide range of variances by varying a and b from 10^{-6} to 10^0 (smaller variances), and from 2^0 to 2^7 (larger variances), using exponential step sizes of 1. Additional values of $10^{-0.5}$ and $2^{-0.5}$ were also included. This systematic investigation allowed us to visualize the trainable parameter space in a two-dimensional plot, where the x- and y-axes correspond to the variances of the forward and backward weights, respectively.

Next, we examined the effect of network depth on trainability. We trained multi-layer feedforward networks with depths ranging from 2 to 10, keeping the hidden layer size fixed at 512 units. All other conditions—including weight initialization, training dataset size, optimizer, and hyperparameters—were identical to those used in the main experiments.

Finally, we tested trainability under limited data conditions. We trained three-layer feedforward networks on subsets of the training data ranging from 100 to 50,000 samples. Again, all other training conditions were kept consistent with those used in the main experiments.

B.6 Visualization of trajectory in loss landscape

To visualize the optimization trajectory within the loss landscape [43], we recorded the model parameters θ_i at each training step and flattened them into one-dimensional vectors. We then constructed a matrix of difference vectors:

$$[\theta_0 - \theta_{\text{final}}, \theta_1 - \theta_{\text{final}}, \theta_2 - \theta_{\text{final}}, \dots],$$

where each column represents the deviation of the parameter vector at a given step from the final converged model θ_{final} . Principal Component Analysis (PCA) was applied to this matrix to identify the two principal directions that explain the most variance in the trajectory. These directions define a two-dimensional subspace within the high-dimensional parameter space. To visualize the loss surface, we interpolated model parameters across a grid within this subspace and computed the corresponding training loss values, thereby constructing a two-dimensional loss landscape. The optimization trajectory was projected onto the same subspace and overlaid on the loss surface, providing a geometric visualization of how the model navigates the loss landscape during training.

B.7 Spectral analysis on Hessian of loss

To quantitatively analyze the stability of the learning trajectory and the characteristics of converged optima, we investigated the geometric properties of the loss landscape by performing spectral analysis using the Hessian of the loss. Since we mainly considered neural networks for image classification tasks, we define the network as f_θ , parameterized by $\theta = \{\mathbf{W}_l, \mathbf{b}_l\}_{l=0}^{L-1}$, and optimized to minimize the loss function $\mathcal{L}(\theta)$. The gradient and second derivative of the loss with respect to model parameters, i.e., the Hessian, are given by:

$$g_\theta = \frac{\partial \mathcal{L}}{\partial \theta}, \quad H_\theta = \frac{\partial^2 \mathcal{L}}{\partial \theta^2} = \frac{\partial g_\theta}{\partial \theta}.$$

However, due to the large number of parameters in deep neural networks, explicitly computing the full Hessian matrix is computationally infeasible. Therefore, we analyzed the spectral properties of the Hessian without explicitly forming it, using approximate and iterative methods as proposed in previous research [44]. In particular, this can be achieved by computing the product of the Hessian and a random probe vector $v \sim \mathcal{N}(0, I)$. This product, $H_\theta v$, can be efficiently computed by backpropagating the inner product $g_\theta^\top v$, using the identity:

$$\frac{\partial g_\theta^\top v}{\partial \theta} = \frac{\partial g_\theta^\top}{\partial \theta} v + g_\theta^\top \frac{\partial v}{\partial \theta} = \frac{\partial g_\theta^\top}{\partial \theta} v = H_\theta v.$$

We used power iteration to compute the top eigenvalue of the Hessian [61]. Next, we computed the trace of the Hessian using a randomized numerical linear algebra method [62]. The trace is computed using the identity:

$$\text{Tr}(H_\theta) = \text{Tr}(H_\theta I) = \text{Tr}(H_\theta \mathbb{E}[vv^\top]) = \mathbb{E}[\text{Tr}(H_\theta vv^\top)] = \mathbb{E}[v^\top H_\theta v],$$

where v is a random probe vector. Since $v^\top H_\theta v$ is the dot product between $H_\theta v$ and v , the trace can be estimated by averaging this quantity over multiple samples. We also estimated the empirical spectral density (ESD) of the Hessian using the stochastic Lanczos quadrature (SLQ) method [63, 64]. The ESD is defined as

$$\rho(\lambda) = \frac{1}{m} \sum_{i=1}^m \delta(\lambda - \lambda_i),$$

where λ_i are the eigenvalues of the Hessian matrix. Since computing all eigenvalues is intractable, we approximate $\rho(\lambda)$ by convolving it with a Gaussian kernel, resulting in a smoothed estimate of the density. To compute this efficiently, we apply the Lanczos algorithm to Hessian-vector products using multiple random probe vectors. This yields a tridiagonal matrix whose eigenvalues and weights approximate those of the original Hessian. The final estimate of the smoothed spectral density is given by:

$$\rho_\sigma(t) \approx \frac{1}{n_v} \sum_{l=1}^{n_v} \sum_{i=1}^q \tau_i^{(l)} \cdot \frac{1}{\sigma \sqrt{2\pi}} \exp\left(-\frac{(t - \lambda_i^{(l)})^2}{2\sigma^2}\right),$$

where $\lambda_i^{(l)}$ and $\tau_i^{(l)}$ are the eigenvalues and associated weights from the l -th Lanczos run, and n_v is the number of random probe vectors used. Throughout our spectral analysis, we utilized and modified code provided by previous research [44].

B.8 Perturbed loss landscape analysis

To evaluate the stability and smoothness of the converged solution, we analyzed the perturbed loss landscape around the final model parameters. After convergence, we computed the top two eigenvectors of the Hessian of the loss function, corresponding to the largest eigenvalues. These eigenvectors define the principal directions of curvature in the parameter space. We then constructed a

two-dimensional subspace by perturbing the converged parameters along these directions. Specifically, for scaling parameters α and β , the perturbed parameters were defined as:

$$\theta_{\text{perturbed}} = \theta_{\text{final}} + \alpha\lambda_1 + \beta\lambda_2,$$

where λ_1 and λ_2 are the eigenvectors associated with the largest and second-largest eigenvalues, respectively. The point $(\alpha, \beta) = (0, 0)$ corresponds to the unperturbed test loss at the converged solution, while losses evaluated at other points reflect the model’s sensitivity to perturbations in parameter space. A relatively flat loss landscape—where test loss remains low even under substantial perturbations—indicates that the solution resides in a wide, stable minimum. Conversely, a sharp increase in loss with small perturbations suggests that the solution lies in a narrow or sharp minimum, which may be associated with poorer generalization and greater sensitivity to parameter variations.

B.9 Corruption robustness

To assess the model’s robustness against input corruptions, we evaluated its performance on the CIFAR-10-C dataset [50] after training on the clean CIFAR-10 dataset. CIFAR-10-C includes 15 types of corruptions that mimic real-world data degradation, grouped into four categories: (1) Noise — Gaussian noise, shot noise, impulse noise; (2) Blur — defocus blur, glass blur, motion blur, zoom blur; (3) Weather — snow, frost, fog, brightness; and (4) Digital — contrast, elastic transformation, pixelation, JPEG compression. Each corruption type is offered at five severity levels, ranging from 1 (least severe) to 5 (most severe). In the main analysis, we employed severity level 1 to represent mild yet realistic distortions. Results for all severity levels are provided in the Supplementary Results. Robustness was measured using the mean corruption accuracy, calculated by averaging classification accuracy across all corruption types at a specific severity level. A higher mean corruption accuracy signifies that the model retains reliable performance across a broad range of corruptions, indicating improved generalization to distributional shifts.

B.10 Adversarial robustness

To assess the robustness of the neural network against adversarial attacks, we employed the Fast Gradient Sign Method (FGSM) [51]. FGSM generates adversarial examples by adding perturbations in the direction that maximally increases the loss. Given an input x , label y , and loss function $\mathcal{L}(x, y)$, the adversarial example is constructed as:

$$x_{\text{adv}} = x + \epsilon \cdot \text{sign}(\nabla_x \mathcal{L}(x, y)),$$

where ϵ controls the magnitude of the perturbation. We evaluated adversarial robustness by varying ϵ from 0 to 0.05 and measuring the corresponding test accuracy on the perturbed inputs. A steep decline in accuracy with increasing ϵ indicates vulnerability to adversarial perturbations, whereas more stable accuracy suggests stronger robustness.

C Experimental details

C.1 Data availability

The datasets used in this study are publicly available: <https://www.cs.toronto.edu/~kriz/cifar.html> (CIFAR-10 and CIFAR-100 [40]), <http://ufldl.stanford.edu/housenumbers/> (SVHN [39]), <https://cs.stanford.edu/~acoates/stl10/> (STL-10 [41]).

C.2 Code availability

Python 3.12 (Python Software Foundation) with PyTorch 2.1 was used to perform the simulation. The code used in this work will be made available after the paper is published.

C.3 Computing resources

All simulations were performed on a computer with an Intel Core i9-13900K CPU and an NVIDIA GeForce RTX 4090 GPU. The simulation code was parallelized using PyTorch's built-in parallelization to utilize the GPU resources efficiently.